NASA CR-135212

SURFACE ASPECTS OF PITTING AND STRESS CORROSION CRACKING

by

J.J. Truhan, Jr. and R.F. Hehemann

CASE WESTERN RESERVE UNIVERSITY
Cleveland, Ohio

Final Report
for Period September 1974 to March 1977

Prepared for

NATIONAL AERONAUTICS AND SPACE ADMINISTRATION
NASA LEWIS RESEARCH CENTER

Grant NGR 36-027-051
April 1977

NASA CR-135212

SURFACE ASPECTS OF PITTING AND STRESS CORROSION CRACKING

by

J.J. Truhan, Jr. and R.F. Hehemann

CASE WESTERN RESERVE UNIVERSITY
Cleveland, Ohio

Final Report
for Period September 1974 to March 1977

Prepared for

NATIONAL AERONAUTICS AND SPACE ADMINISTRATION
NASA LEWIS RESEARCH CENTER

Grant NGR 36-027-051
April 1977

1. Report No.	2. Government Accession No.	3. Recipient's Catalog No.
NASA CR-135212		

4. Title and Subtitle	5. Report Date
Surface Aspects of Pitting and Stress Corrosion Cracking	6. Performing Organization Code

7. Author(s)	8. Performing Organization Report No.
J. J. Truhan and R. F. Hehemann	10. Work Unit No.

9. Performing Organization Name and Address	11. Contract or Grant No.
Case Western Reserve University Cleveland, Ohio 44106	NGR 36-027-051

12. Sponsoring Agency Name and Address	13. Type of Report and Period Covered
National Aeronautics and Space Administration Washington, D.C. 20546	Final Report 9/74 - 3/77
	14. Sponsoring Agency Code

15. Supplementary Notes

Project Managers, Charles W. Andrews and Hugh R. Gray
Materials and Structures Division
NASA, Lewis Research Center, Cleveland, Ohio 44135

16. Abstract

The pitting and stress corrosion cracking of a stable austenitic stainless steel in aqueous chloride environments were investigated using a secondary ion mass spectrometer as the primary experimental technique.

The surface concentration of hydrogen, oxygen, the hydroxide, and chloride ion, magnesium or sodium, chromium and nickel were measured as a function of potential in both aqueous sodium chloride and magnesium chloride environments at room temperature and boiling temperatures. It was found that, under anodic conditions, a sharp increase in the chloride concentration was observed to occur for all environmental conditions. The increase may be associated with the formation of an iron chloride complex. Higher localized chloride concentrations at pits and cracks were also detected with an electron microprobe. The above results confirm the theories that the chloride ion attacks the passive film of the stainless steel locally leading to pitting and cracking commonly observed in this system.

The role of hydrogen as a mechanism for stress corrosion cracking was investigated by comparing hydrogen concentrations on the free surfaces in contact with the environment and a fracture surface. Higher than background concentrations of hydrogen were commonly observed on the free surface for strong cathodic polarization but generally the increase was not a large one. On the fracture surface, however, a substantial increase in the concentration of hydrogen was detected. This observation tends to support the hydrogen embrittlement mechanism for stress corrosion cracking.

17. Key Words (Suggested by Author(s))	18. Distribution Statement
Hydrogen analyses Austenitic Stainless Steels Stress Corrosion Cracking Ion Probe Mass Spectrometer Pitting	Unclassified - unlimited

19. Security Classif. (of this report)	20. Security Classif. (of this page)	21. No. of Pages	22. Price*
Unclassified	Unclassified	88	$4.75

* For sale by the National Technical Information Service, Springfield, Virginia 22151

INTRODUCTION

Stress corrosion cracking (SCC) is the simultaneous action of a tensile stress and an aggressive environment on an alloy system to produce a brittle fracture in a normally ductile material at stress levels far below engineering design limits. The stress can be externally applied or it can be an internal residual stress. SCC is also highly specific in that there is no universal environment observed as yet that will produce the phenomenon in all alloy systems. What is an aggressive environment for one alloy system may leave another unaffected. All of these characteristics make SCC one of the most insidious problems for the design engineer to deal with.

The phenomenon of SCC was first observed in the nineteenth century with the failure of cold worked brass shell caseings in atmospheres containing traces of ammonia (1). The SCC of the austenitic stainless steels in aqueous chloride environments has been recognized for about fifty years with the first work published in 1940 (2). Since the austenitic stainless steels in chloride solutions are so economically important, this system has been the subject of intensive research ever since it was first recognized. Much empirical data has been previously recorded, but no universally accepted mechanism has been proposed to satisfactorally explain all of the observed data. For these reasons, this system was chosen for the subject of this study. Improved

experimental techniques now available allow for the examination of the phenomenon of SCC on a more fundamental level.

SCC has been traditionally divided into two major aspects, crack initiation and crack propagation. The major concern of this study will be the crack initiation aspect, ie., what conditions must exist at the alloy environment interface to initiate cracks and how are these conditions affected by various environmental parameters?

It has been commonly observed that a very close relationship exists between SCC and pitting, so that any discussion of the crack initiation aspects of SCC must include the description of mechanisms involved in the pitting process also.

In an attempt to explain the mass of empirical data accumulated to date, various mechanisms have been proposed. Several of the more popular explanations will be briefly outlined here. More complete summaries of the currently accepted mechanisms can be found elsewhere (3-5).

1. The Dissolution Model

The dissolution model explains the localized attack on the surface of an alloy on the basis of small areas which are anodic with respect to the surrounding matrix. Such areas have been identified as metal carbides (6), sulfide inclusions (7,8), grain boundaries (9,10), and deformed material (1). It has also been

thought that areas depleted in chromium can lead to localized attack by depriving the base material of a protective coating (9). Pitting corrosion studies have also identified pits as local anodes (11). This essentially electrochemical theory has some merit, but is inadequate in explaining the effect of stress and the observation of transgranular failures.

2. The Dislocation Structure Model

It has been observed by Staehle, Scully and others that many alloys which are susceptible to SCC, including the austenitic stainless steels have low stacking fault energies (SFE) (4,5,12). In these cases, cross slip is difficult and essentially a widely spaced planar array of dislocations results. Another factor influencing the dislocation structure in the austenitic stainless steels is the presence of short range order (SRO) which, like low SFE, confines the dislocations to planar arrays (12). The planar arrays then move under the application of stress and eventually emerge on the surface as slip steps which are subject to localized attack by interrupting a protective surface film (13,14). The catalytic activity of dislocations and dislocation pileups cutting the surface imply likely regions for localized dissolution (15). Furthermore, the existence of SRO could lead to compositional changes on the surface which could create a local anode.

Scully has indicated that the susceptibility of an alloy in a particular environment depends on the kinetics of repassivation of the newly exposed surfaces (13,14). This model accounts for both the localized attack necessary for crack initiation and the effect of stress. It holds much attraction except for the observation (12) that alloys such as Incoloy 800 which meet the model's criteria are not susceptible as predicted.

3. The Adsorption Model

This model for SCC, principally supported by Uhlig (16), states that the adsorption of a damaging species lowers the surface energy of the alloy allowing for easier decohesion and hence, accelerated attack. As a result of pitting corrosion research by a number of investigators (17-19), the chloride ion has been identified as the species which attacks or breaks down a protective film leading to localized dissolution. Protective or passive film, in this context, should not be restricted to mean an oxide layer, but any covering which blocks the base metal from the environment. Recent experimental work done by Vetter and associates (20-23), on iron and nickel show localized chloride concentration at pit sites. Rideout and coworkers, in electron microprobe studies of hot salt stress corrosion cracking of titanium based alloys have shown not only high chloride concentration around the stress corrosion cracks but also a correspond-

ing high sodium concentration as well (24).

A mechanical extension of this model recently updated by Vermilyea and coworkers (25) theorize that a brittle film exists on the surface which is broken under stress, exposing localized areas of the base metal to the environment.

It has been noted by Scully (13) that stressing changes the morphology of the pits from wide shallow ones to deep narrow pits or crack nuclei. But as he later pointed out (14), SCC requirements must be stringent since it has been generally observed that while alloys susceptible to SCC in a particular environment will pit in the absence of stress, not all systems which pit will crack when stressed. This model does not account for the varying degrees of susceptibility of the austenitic stainless steels in different chloride environments. As an example, it has been generally observed that the austenitic stainless steels are more susceptible in magnesium chloride environments than in sodium chloride environments of the same concentration (26,27). These differences have yet to be satisfactorally rationalized at this time.

4. The Hydrogen Model

The many similarities between the phenomenon of hydrogen embrittlement (HE) and SCC such as brittle delayed failure, have lead to the development of an HE mechanism for SCC by Troiano,

Nielson (28), Vaughn (29) and others. Although it was thought for some time that the face-centered cubic alloys were generally immune to HE, it has been shown to occur in aluminum alloys (30), monels (31) and the austenitic stainless steels (32). Troiano and associates (33-35) have demonstrated that hydrogen will permeate through an austenitic stainless steel under anodic conditions in acid and chloride environments if and only if pitting occurs. This has been attributed to a drop in pH at the base of a pit giving a high concentration of available hydrogen. A more detailed account of the electrochemical processes occurring in pits and cracks is given by Ateya and Pickering (36). The experimental evidence of hydrogen permeation through an austenitic stainless steel under a net anodic potential when, electrochemically, hydrogen evolution is not expected to occur on the metal surface shows that a great deal of consideration must be given to reactions on a local cell level. Furthermore, the effect of stress is accounted for in that it would assist the transport of hydrogen to critical areas possibly by a dislocation dragging mechanism (37-39). Considering the slow diffusion rate of hydrogen through a face-centered cubic lattice (33), applied stress may be necessary to achieve adequate transport rates explaining the coaction of stress and environment.

A major objection to an HE mechanism for SCC in the austeni-

tic stainless steels is the small ductility loss observed after cathodic charging (4). There is also some disagreement as to whether HE and SCC are two separate and distinct phenomena or one and the same effect.

Due to the extreme complexity of the phenomenon of SCC, it is conceivable that no unified theory will ever be formulated using a single simple model. Indeed, due to the experimental verification of such widely diverse processes as hydrogen embrittlement, adsorption, and localized anodic dissolution occurring during SCC, it is possible that all of the above occur simultaneously to varying degrees. The principle process involved in a particular alloy-environment combination might well be determined by the kinetics of each of the individual processes.

Although no model currently enjoys universal acceptance in describing an operable mechanism for SCC, all models share a common obvious feature, ie., in the initiation process of SCC, the reactions at the metal-environment interface are of extreme importance. Up until relatively recently, these surface reactions were deduced indirectly from the response of a material to changes in environmental parameters by using engineering parameters such as times to failure. At the present time, however, experimental techniques are available which allow for the direct determination of the various surface reactions. The

techniques include the electron microprobe, Auger spectroscopy, low energy electron diffraction and secondary ion mass analysis. These techniques are described in a recent paper by Benninghoven (40).

This research employed the secondary ion mass spectrometer (SIMS) as the principle experimental tool. A more detailed description of the instrument will be given later. The ability of the SIMS to distinguish the light elements easily makes it a particularly suitable instrument for testing the hydrogen and adsorption models simultaneously during the measurement of surface concentrations.

The electron microprobe and scanning electron microscope were also employed here to a lesser extent in such instances where their capabilities make them particularly suited.

As mentioned earlier, these techniques were applied to the study of pitting and the crack initiation phase of SCC of a stable austenitic stainless steel in aqueous chloride environments. AISI type 310 stainless steel was chosen as the alloy to be examined because the high nickel content stabilizes the austenite and eliminates the martensite reaction. The presence of a nonuniform distribution of martensite would add a complicating factor at this time. Magnesium chloride and sodium chloride environments were chosen because of their chemical similarity yet different behavior in SCC. This research will

attempts to point out the differences between the two environments which could account for their dissimilar behavior.

MATERIALS AND APPARATUS

In all experiments, a commercial grade type 310 stainless steel from a single heat was used. The chemical analysis for the heat is given in Table 1. The steel was supplied in a bright annealed sheet form. A slight amount of cold working resulted from the coiling operation, but no attempt was made to reanneal. Light micrography in Figure 1 shows the grain structure to still be equiaxed. Tensile data included in Table 1 shows also that the amount of cold working was slight.

The solutions were prepared from single lots of ACS certified grade chemicals in distilled water and were unbuffered. Single lots of both alloy and chemicals were employed to minimize spurious effects of trace elements. The solutions were prepared for concentrations of 5M sodium chloride and 2.5M magnesium chloride of dry salt in order to obtain a constant chloride concentration between the two salt solutions. The pH of the solutions ranged from 5.5 to 6 with the magnesium chloride solutions slightly more acidic.

The electrochemical polarization of the specimens was carried out with a Wenking Potentiostat Model 70 TS1. To facilitate the recording of polarization curves, a Wenking SMP 72 Scanning Potentiometer was used in conjunction with the potentiostat to change the amount of overvoltage at a fixed, predetermined rate. Potentials were measured using a platinum counter electrode with respect to a saturated calomel electrode (SCE) isolated from the test solu-

tion by a salt bridge of the same composition as the solution. Figure 2 illustrates the experimental arrangement.

The major part of the surface analysis was carried out with a GCA secondary ion mass spectrometer (SIMS). Figures 3 and 4 show the instrument. The SIMS combines a sputter ion source and a mass spectrometer. Detailed descriptions of the theory and construction are available in the literature (41-45). A duoplasmatron ion source produces a beam of ions which are accelerated through a system of electrostatic lenses to the sample stage below. The sample to be analyzed is mounted at 45° angle to the incident primary beam. Surface components are sputtered off of the sample and the charged secondary ions, along with the reflected primary beam, are accelerated through a second set of electrostatic lenses into the mass spectrometer section. The mass spectrometer is of the Mattauch-Herzog double focusing type. The design and optics of this particular type of mass spectrometer are described by Herzog elsewhere (46). The double focusing capabilities refer to separate electrostatic and magnetic sectors. The electrostatic sector serves as an energy window to produce a monoenergetic beam of ions for mass analysis. This feature allows for uniform sensitivity over the entire mass range.

In order to examine concentration gradients on the surface on a microscale, an ARL electron microprobe EMX-SM was used since the electron beam diameter is on the order on one micron or less. In

contrast, the beam diameter for the GCA SIMS is on the order of millimeters.

Surface details of cracks and pits were observed with a JEOL scanning electron microscope (SEM) Model JSM 2 which has been equipped with capabilities for the energy dispersive analysis of x-rays.

EXPERIMENTAL PROCEDURE

1. Electrochemical Polarization

Two types of polarization experiments were carried out. First was the determination of the polarization curve for each of the environmental conditions of interest. The second type of polarization experiment involved holding a sample at a constant arbitrary potential for subsequent analysis in the SIMS to determine the concentration of various species present on the surface as a result of that treatment.

For all polarization experiments, the samples were prepared in an identical manner. No more than one hour prior to immersion in the test cell, the steel was wet ground with 600 grit silicon carbide paper, rinsed in ethanol and air dried using a heat gun. All other surfaces and leads which were not to be in contact with the test solution were coated with a fast drying lacquer. After the sample was placed in the cell and all leads were connected, it was allowed to equilibrate for one hour. After this time, it was found that the open circuit or rest potential, E_r, had stabilized. If the solution was to be deaerated, this was done for at least twelve hours previous to the test by bubbling argon through the solution using a fritted glass disperser. Any aeration of the solution was done by introducting oxygen into the solution during the rest potential stabilization period. The overvoltage

for a constant potential experiment was applied for one hour, after which time, it is believed, conditions on the surface would be in equilibrium. After this experiment, the samples were removed from the solution, washed briefly first in distilled water and then in ethanol, air dried and mounted for analysis. The washing procedure was arrived at by trial and error and is thought to be the best compromise in removing artifacts without unduly disturbing the surface.

Unless indicated on the figures, all polarization was done on unstressed specimens. Specimens that were stressed for constant potential analysis were stressed using a two point bending method similar to that described by Heimerl and Braski (47). The samples were stressed just below the yield point. To obtain stress corrosion cracked specimens for EMX and SIMS analysis, the samples were stressed in uniaxial tension by a constant load in a cantilever beam arrangement (35).

Polarization curves were obtained using a step wise potentiostatic method in which the overvoltage was changed in small fixed increments while monitoring the current. For cathodic polarization, the scan rate was 15 millivolts per minute and for anodic polarization, the scan rate was 3 millivolts per minute. The same procedures for sample preparation and equilibration as for the constant potential samples were followed here as well.

Surface analysis with the SIMS was carried out using techniques developed earlier by the author (48). High purity argon was used as the primary beam since no chemical reaction between the beam and the sample would be expected to occur during the sputtering process. The primary instrument parameters were kept constant throughout this investigation and are summarized in Table 2. For normal operation, secondary ions that are analyzed are positive species. Modification to the SIMS prior to this investigation allowed for the detection of negative species as well. It was felt that the modification would allow for more sensitive detection of species such as oxygen, the hydroxyl and chloride ions which readily pick up electrons and are not expected to ionize as positive species to any great extent. To minimize errors in the detected concentrations due to sputtering time effects, specimens that were cathodically polarized were first analyzed for the positive species. In this manner, any possible hydrogen pickup would be detected quickly. Analysis for negative species would then be carried out on an undisturbed area of the sample. The reverse procedure was used for samples anodically polarized for the detection of the chloride ion and oxygen and hydroxyl ions as well. Some sputtering time effects are bound to occur, but this method minimizes these effects. Each mass species of interest was checked for maximum focus conditions rather than maintaining constant focus conditions. Although much care was taken to insure that the instru-

ment parameters were kept constant from analysis to analysis, small variations, some due to electronic drift, occur sometimes to yield large effects on a log scale. For this reason, all intensities reported here are normalized relative to the detected iron peak for that particular analysis. Since iron is the main matrix element in type 310 stainless steel, it is assumed that fluctuations in iron concentrations are minimal. Also, the relatively large beam diameter would tend to integrate out any differences on a microscale.

The large beam diameter of the SIMS made it unsuitable for the detection of preferential adsorption of any species on a microscale. An EMX was employed in these instances due to the less than one micron beam diameter. For best results in the surface analysis where coatings were expected to be of atomic dimensions, the accelerating voltage of the EMX was reduced to 5 kilovolts. The low primary accelerating voltage minimized electron beam penetration. It was found earlier that higher voltages "smeared out" any surface variations.

RESULTS AND DISCUSSION

1. Polarization Curves

The polarization curves for the conditions of interest are given in Figures 5 through 12. Several features should be noted here. The first obvious feature is that these systems do not exhibit classic active passive behavior as for the austenitic stainless steels in acid environments. The active passive behavior of the austenitic stainless steels in aqueous chloride environments has been noted by Ro (35), d'Erceville (49), and Staehle (4). d'Erceville has shown that for increasing chloride concentrations, the passive potential range decreases, probably due to instabilities of the passive film. For the concentrations used in this study, the active range is totally obscured and there is only evidence of a very small quasi passive range at room temperature due to the high reduction reaction. The structure and properties of the passive film of an austenitic stainless steel are given by Okamoto (50).

This can be more clearly illustrated by the following description. The classic active passive polarization curve is illustrated in Figure 13a with the regions appropriately labeled. As the potential is made more noble the current rapidly increases in the active region until a passivating potential Epp is reached. At this point, a passive film formation occurs which blocks the

alloy from the environment as evidenced by the drastic drop in current. This passive film is usually stable over a large potential range. As the potential E_b is reached, localized breakdown of the film lead to the creation of local anodes surrounded by relatively large cathodic areas and pitting results.

In Figure 13b, a hydrogen reduction reaction is superimposed on the oxidation reaction which intersects the oxidation reaction in the passive region only. In the absence of applied potentials, the alloy is spontaneously passivated in this environment. At a given potential, both the oxidation and reduction reactions are occurring simultaneously. A potentiostat measures the net current difference, anodic for applied potentials more noble than the rest potential and cathodic for potentials more active. For overvoltages farther from the rest potential the contribution of the lower current reaction is slight due to the large current differences. The resultant current-potential curve as actually measured experimentally is illustrated in Figure 13c.

Electrochemical breakdown of the stable passive layer occurs at potentials far more noble than potentials applied in this study as indicated in the Appendix. Local film breakdown leading to pitting attack probably occurs initially by adsorption and the dissolution of anodically active precipitates on the surface. For the anodic branch of the polarization curves determined here, the anodic current is an average of the relatively low rate of attack

on the passive film and the high rate of attack at pits. As the pitted surface area increases, this contribution to the anodic current increases also. Therefore, while a true breakdown potential is never reached pitting occurs and a transpassive region is observed on the anodic branch none-the-less. Okamoto (50) shows the destruction of the protective film due to the chloride adsorption process. A complicating factor experimentally is the rapidly increasing surface area due to pitting. Customarily, current density is indicated on the polarization curve but when pitting is occurring, this can only be approximate.

For cathodic polarization, the break in linearity of the hydrogen reduction reaction may be due to the relatively larger contribution of the oxidation reaction at the "knee" of the curve. As the potential becomes more active, this contribution to the net current rapidly decreases and the cathodic polarization branch becomes linear as expected.

The above discussion assumes single processes only. If, as done here, oxygen is deliberately added to the environment, an additional reduction reaction is added so that the total reduction reaction is shifted in the noble direction.

The major differences between this set of curves in Figures 5 through 12 seems to be in the movement of the rest potential E_r. The effect of the various environmental parameters will be summarized here.

a) For both the sodium chloride and magnesium chloride environments, the additions of oxygen to the environment shifts the rest potential in the noble direction as compared to the corresponding deaerated condition. This is not unexpected, since the addition of oxygen adds an additional reduction reaction which increases the total reduction current for a given potential. Thus, the rest potential becomes more noble.

b) Increasing the temperature to the boiling point leads to a shift of the rest potential for both sodium and magnesium chloride in the active direction.

c) Consistent shifts in the rest potential between corresponding conditions of temperature and aeration for the two salts are difficult to ascertain. This may mean that the polarization behavior is more dependent on the concentration of the anion in the solution. Since chloride concentrations for sodium and magnesium chloride solutions are the same, the rest potential in each case is roughly equal.

The effect of aeration on the anodic polarization for the sodium and magnesium chloride environments is evident at low current densities. The cathodic polarization shows major shifts to higher currents due to the addition of the oxygen reduction reaction. At boiling temperatures, however any differences between the aerated and deaerated conditions are seen to be slight probably because of the boiling action which automatically deaerates the solution.

The polarization curves were used to choose appropriate experimental conditions and appropriate potentials for the constant potential polarizations for surface analysis. The interpretation of these polarization curves to obtain corrosion and pitting information is given by Greene (51,52).

It should be noted here that the deaeration technique using an inert gas to force the oxygen out of solution by the artificial boiling action may not be completely adequate. ASTM recommended practice for the determination of polarization curves dictate the use of hydrogen as a deaeration agent (53), but this was not done for safety reasons.

2. Surface Analysis with the SIMS

Table 3 shows the average background intensities for several nominally clean unpolarized samples. As noted earlier, all intensities are normalized with respect to an iron peak to account for instrument differences from experiment to experiment.

In the early stages of these experiments, SIMS analysis of the constant potential conditions were repeated two or three times each in order to determine the degree of repeatability. In general, it was noted that the detected intensities of the main matrix elements for clean samples varied by $\pm$ 0.1. Background intensities for trace elements such as hydrogen and oxygen showed a little more variation. While little significance should be attached to the

actual intensities recorded here, for the reasons given later, the trends that were noted were highly repeatable.

Typical mass scans for type 310 stainless steel anodically polarized in the magnesium chloride solution for both the positive and negative ions are shown in Figures 14 and 15. One should note the drastic improvement in the detection of the chloride, hydroxyl, and oxygen ions by scanning the negative ion spectrum in Figure 15. Without the ability to detect these negative ions, the SIMS would have been useless in this application. Emphasis should be made at this point that the relative intensities shown here for different ions are not an indication of relative concentrations. For example, the fact that the chromium peak is larger than the iron peak does not mean that a greater amount of chromium exists in the alloy. Quantitative estimates may be made if accurate values for the sputter yields for an element in a particular matrix can be determined. To date, the physics of sputtering is not developed to the point that a good description can be given of the process. All data which will be presented then are uncorrected for sputter yields.

Cathodic Polarization

No variation of oxygen or the hydroxyl radical with potential was observed and the levels detected were essentially background

levels for both the aerated and deaerated conditions in both salt solutions as shown in Figures 18 through 23. Some of this background can be attributed to traces of moisture in the vacuum system, some to adsorbed moisture picked up on the sample during loading into the SIMS and some to an oxide coating.

There was usually a small increase of hydrogen observed on the surface at more active potentials for all conditions. The hydrogen intensity could be observed to decrease with more noble potentials. No differences in hydrogen adsorption can be seen between the two salt solutions. The sensitivity of the SIMS to hydrogen pickup has been previously demonstrated (48) so that if a significant amount of hydrogen adsorption at high active potentials occurred, it would have been noted.

It was usually, but not consistently observed that large amounts of magnesium or sodium were present on the surface at high active potentials.

Anodic Polarization

With evidence of only a weak quasi passive film, as shown by the polarization curves, pitting was observed to occur at even small overvoltages, the pit density determined by the amount of anodic current. SEM photomicrographs in Figures 16 and 17 shows that the pits are irregular but generally hemispherical, especially in the initial stages. It should be noted here that, for even

severely pitted surfaces, no general corrosion is observed to have occurred with the original polishing scratches still intact.

SIMS examination shows in Figures 18 through 23, a sharp increase in the amount of chloride detected for anodic potentials. This occurred consistently for all environmental conditions. At more noble potentials, a decrease in the chloride intensity occurs. Since this occurs for most conditions and was verified several times, the decrease is assumed to be real. The instances where the chloride concentration did not decrease occurred for potentials closer to the rest potential. This probably arises for several reasons. First desorption due to ionic repulsion after a maximum surface concentration is reached could occur. It would not be reasonable to expect to observe increasing surface concentrations with increasing noble potentials but rather a saturation limit instead. A second reason for the decrease is due to the high anodic current at high noble potentials which implies a high dissolution rate which would destroy existing surface conditions.

Possible surface reactions occurring for austenitic stainless steel in an aqueous chloride solution are listed in the Appendix along with the equilibrium potential for each reaction. Extensive data for these reactions are available at room temperature only.

One should note that the maximum chloride concentrations for

both salt solutions at room temperature occur at potentials that correspond closely to the equilibrium potentials for iron chlorides formation. The adsorption process may be described as a two stage process in which physical adsorption is followed by chemical bonding to form "surface molecules" at a given potential. Vetter and Strehblow (22) have advanced the idea that active metal is not exposed directly to the environment during the pitting process but is covered by an iron chloride salt covering. The relationship between the increase in chloride concentration and the equilibrium potential for iron chloride formation tends to support this theory.

Data concerning the ionic conductivity of the chloride complexes are not generally available, but it is assumed that an iron chloride layer in an amorphous form on the surface would not inhibit ion transfer and, hence, not act as a protective film as would an oxide.

Research by Gerasimov and coworkers (54) using autoradiography techniques has shown a similar behavior to the results in this study for the adsorption of the chloride ion on type 304 stainless steel. Increasing chloride adsorption was observed for anodic potentials up to the breakdown potential after which a decrease was seen. The relationship between the adsorption of the chloride ion and the onset of pitting or cracking observed by many previous workers appears to be verified in this study.

An unexpected result was the detection of either a high magnesium or sodium concentration under anodic conditions. From classical electrochemical theory, one would not expect the adsorption of positive ions for net anodic conditions on the surface. This effect was again consistently observed for all environmental conditions. One possible explanation for this phenomenon might be that the chloride ions attract the positive ions from the solution to maintain charge neutrality on the surface after the applied potential was removed at the termination of an experiment. The use of the SCE made it impossible to maintain the applied potential during sample removal. It is difficult to ascertain then whether this electrodeposited "salt" coating is a real effect or an artifact due to sample handling. It was consistently observed and appeared to be adsorbed strongly enough to survive the sample washing in distilled water prior to analysis in the SIMS. Another reason that this effect is a real one is the fact that the reverse situation is not seen, ie., for high active potentials, where higher levels of sodium or magnesium were detected, no corresponding high levels of the chloride ion are observed.

No differences in oxygen level were observed between the aerated and deaerated conditions for either the magnesium chloride or sodium chloride solutions. Due to fluctuations in background any oxygen effects were difficult to observe and no evidence can be seen for any competitive adsorption process with the chloride ion.

According to recent work by Vacarro (27), aeration has little effect on failure times for 310 austenitic stainless steel in magnesium chloride solutions. Since very little effect is seen with the addition of oxygen in this study, this result is easy to rationalize. In early work by Edelenau (26), it was found that the addition of oxygen to sodium chloride solution induces SCC susceptibility in the austenitic stainless steels but failure times are still very long. The effect of the additional reduction reaction might be sufficient to increase the equilibrium potential above the cracking potential so that cracking occurs. In either case the addition of oxygen to the solution has only a slight effect on SCC behavior and is reflected by the relative oxygen levels determined here.

As the temperature was increased, no substantial increases in chloride ion intensities were observed compared to room temperature. On the other hand, a consistently large increase of magnesium was observed at high temperature but a similar increase for sodium was not seen. This different behavior might be attributed to film formation accelerated by the high temperature in the magnesium chloride solution. Magnesium hydroxide has been commonly observed to form during SCC, but no increase in the hydroxyl radical is consistently observed here.

Chromium and nickel intensities are also plotted as a function of potential for the deaerated conditions for both ambient and boiling temperatures in Figures 18b, 20b, 21b and 23b. With the exception of the boiling magnesium chloride environments in Figure 23b, little variation in intensity for both species over the whole potential range is observed.

Although the idea has been abandoned by Staehle (4), there may be some evidence for nickel enrichment for more noble potentials since an increase in the nickel concentration is seen for all cases except for the boiling sodium chloride environment. This is a reasonable result since nickel is more noble than iron and chromium and hence, will dissolve at a slower rate. An apparent increase may possibly be interpreted as an iron depletion at more noble potentials.

Two possibilities exist for the form in which the nickel exists on the surface. First, the nickel may exist as simple metallic nickel. Second, the nickel might be tied up in a surface complex, either a nickel oxide or a nickel chloride or a mixture of the two. A nickel oxide would be stable on the surface normally and a chloride complex might be stable at local noble areas. There is no way to distinguish which of these possibilities is the most likely in this study. Mass scans extended to the higher ranges usually show a great deal of background and it is sometimes diffi-

cult to identify special peaks. No mass peaks were observed which could be satisfactorally identified as either a nickel oxide or a nickel chloride.

With the exception of the boiling magnesium chloride environment, the chromium intensity shows a slight decrease at higher noble potentials. This decrease is consistent with the chromium depletion theory of Joshi and Stein (9).

It should be noted that deviations from the expected trends for both chromium and nickel occur for boiling temperatures in both environments. Whether this observation is significant or merely due to experimental error is not known at this time. The surface reactions determined in the Appendix are for room temperature only because information for these reactions is readily available. The possibility exists that at higher temperatures other surface reactions might occur to explain these results.

3. Concentration Profiles

A unique feature of the SIMS is the ease with which concentration profiles may be determined. With the mass spectrometer fixed for a specific species, the intensity may be monitored as a function of time as successive layers are removed during the sputtering process. With an estimate of the sputtering rate, concentration profiles may be directly determined. An approximate rate of removal for these beam conditions based on previous

estimates is seven to ten microns per hour. Accurate determination of removal rate is difficult due to errosion cones and cratering effects (48). For this reason, only concentration versus time profiles are reported here.

Concentration profiles for stressed and unstressed samples anodically polarized 100 millivolts over the rest potential are shown in Figures 24 through 27. These profiles show the surface effect of the adsorbed species which fall off rapidly to values approaching background levels. Although not plotted here, the iron peak was checked before and after each profile with negligible variation so the higher surface concentrations are not due to possible iron depletion.

There does not seem to be much surface hydrogen but none should be expected under anodic conditions. Higher levels of hydrogen above background after long time sputtering are probably due to edge contributions from the crater which develops. Edge effects were minimized here by using a wide beam of relatively low current density, but cratering is bound to occur in any event and cannot be completely avoided.

One might expect that the intensities for the chloride, sodium, and magnesium ions should decrease to near zero levels after appreciable sputtering times, edge effects notwithstanding, but such is not the case. The use of commercial grade alloys imply the existence of many trace impurities. The sensitivity of

the SIMS to these low concentrations, especially to the more easily ionized elements is about one part in 10^6 to 10^9. As a result, it is probably that a substantial contribution to the intensities after long time sputtering can be due to bulk impurities (55,56).

The effect of stress on the surface concentrations had been an increase of both sodium and magnesium relative to the chloride ion. A dark corrosion film on the sample stressed in the magnesium chloride solution might account for the large increase in the amount of magnesium detected. Surface concentrations of the chloride ion were approximately the same for both the unstressed and stressed sample in the sodium chloride solution and for the unstressed sample in magnesium chloride. The chloride ion showed a large jump in intensity for the stressed sample in magnesium chloride, however, and may be a significant factor in identifying the relative susceptibility of the two salts for the SCC of the austenitic stainless steels. There appears to be some evidence for a stress assisted adsorption effect. Gerasimov (54) had also observed the stress assisted adsorption of chlorides on the surface of a 304 austenitic stainless steel. Since the stressed samples were only exposed for one hour at room temperature no pitting or cracking was observed.

Some results were quite erratic for several stressed samples, but much of this can be attributed to uncertain stress conditions. Two point bending does not seem to be a reliable method for ob-

taining a well defined stress state unless special fixtures are devised. Ideally, the stressing should be done uniaxially.

4. Surface Analysis of Pits and Cracks

To obtain pitted specimens for EMX analysis, anodic polarization in magnesium chloride solutions was employed. A typical traverse for a pit is shown in Figure 28 and similar results were noted for several other pits on the same sample. Figure 28 shows evidence of chloride segregation at the edge of pits similar to that seen by Vetter and associates (20-22) and EMX work for the hot salt SCC of titanium alloys (24).

Stress corrosion cracked surfaces were obtained by loading in uniaxial tension in boiling magnesium chloride polarized 20 millivolts over the rest potential. The traverse across a secondary crack is shown in Figure 29 and a SEM photomicrograph of the typical secondary cracks observed is shown in Figure 30. As with pits, chloride segregation was observed along with small effects of chromium depletion. Due to the results observed here for the constant potential experiments, magnesium was traced across the crack as well. Even on a localized level, higher chloride concentrations had corresponding higher magnesium concentrations associated with them.

As seen in Figure 30, localized dissolution around the secondary cracks exists so that a traverse approaching a crack should

be expected to show essentially the same results as for a pit.

Figure 31 shows the combined intergranular and transgranular nature of the primary fracture surface. SIMS analysis on this fracture surface is summarized in Table 4. A very high hydrogen concentration is shown as well as higher magnesium and chloride concentrations. Nielson (57), using a laser microprobe had observed a similar result for the concentration of hydrogen on the stress corrosion cracked fracture surface of a ferritic stainless steel. The much higher hydrogen on the fracture surface is similar to that noted for cathodically charged monel in which an order of magnitude increase in hydrogen concentration was seen for a fracture surface compared to a free surface (48).

The concentration of hydrogen in both instances followed the same trend, high amounts on the surface rapidly decaying to background levels further into the sample. The similar qualitative results between the fracture surface of the sample cathodically charged to deliberately introduce hydrogen into the lattice and the fracture surface of the sample which had suffered SCC under anodic conditions is suggestive of an HE mechanism for crack propagation in SCC.

During the crack propagation process, new active surfaces are exposed to the environment and hydrogen entry in these areas would not be inhibited. Hydrogen movement through the oxide or hydroxide film is not expected to readily occur. This leads to

high local concentrations of hydrogen at the cracked surfaces as was observed by the SIMS in this study.

The necessity for localized hydrogen entry under anodic conditions is evident when the results of Table 4 is compared with the filmed free surface results in Figure 18 through 23.

One can also see in Table 4 a reduction in the chromium intensity corresponding to the chromium depletion theory of Joshi and Stein (9). In their research using Auger spectroscopy, however, a sensitizing heat treatment produced chromium carbides at the grain boundaries, denuding the surrounding areas of chromium. The annealed sheet used in this study should not be expected to produce as much chromium segregation.

A large increase in the amount of nickel on the fracture surface shows that the nickel enrichment idea of Staehle (4) has merit. Comparison of the results of the EMX and SIMS on the fracture surface shows generally good qualitative agreement, but it must be emphasized that the SIMS integrates a much larger area for analysis due to the beam diameter. The EMX illustrates the segregation around a crack much more satisfactorally.

CONCLUSIONS

A major goal early in this study was the determination of the suitability of the SIMS for surface analysis as applied to corrosion research. After suitable experimental procedures had been devised, it was evident that the instrument could provide valuable information about the surface reactions that occur in the initial stages of SCC. The ability to detect hydrogen constitutes a primary advantage enjoyed by the SIMS technique when applied to SCC phenomenon.

More modern instruments than the model employed in this study contain refinements such as a primary beam approaching EMX dimensions and the ability to raster the beam across the surface giving an "ion picture" for a given species. Fundamental studies of SIMS operation and the physics of the sputtering process are necessary however, in order to obtain reliable quantitative information.

Several conclusions can be stated at this time concerning the crack initiation phase of the SCC of austenitic stainless steels in aqueous chloride environments:

1) The surface concentration of the chloride ion shows a consistently sharp increase for anodic potentials where SCC is observed. The increase in chloride concentration appears to correspond to the formation of an iron chloride complex. A decrease for more noble potentials is observed to occur, probably

due to excessive anodic dissolution.

2) Higher chloride concentrations are observed at pits and cracks. The role of the chloride ion in the initiation of pits and cracks confirms the theories of many previous investigators.

3) High levels of the positive ion, either sodium or magnesium were observed in conjunction with high chloride ion levels both on the overall surface and localized at pits and cracks. The concentration of the sodium ion appears to be relatively independent of temperature whereas the concentration of the magnesium ion increased with increasing temperature. This may be due to a film formation of some sort.

4) No substantial differences in the adsorption characteristics could be observed between the aerated and deaerated condition for both salts. Although no competitive adsorption of chlorine and oxygen could be seen, the additions of oxygen might account for rest potential shifts and film formation as observed in the polarization curves.

5) There is some evidence for a stress assisted adsorption effect which is more pronounced for the magnesium chloride environment than for the sodium chloride environment. This again may be due to some film formation.

6) Although relatively low levels of hydrogen were detected on the overall surface after anodic polarization, a large amount

of hydrogen was observed on a stress corrosion fracture surface generated by the same electrochemical conditions.

7) There is some evidence to support the chromium depletion and nickel enrichment ideas of SCC.

APPENDIX

Surface Reactions and Complex Formations

During the pitting and crack initiation stage of SCC, many surface reactions are assumed to occur simultaneously because of variations in surface potential. Regardless of the applied potential on the overall surface, the potential at a point determines which reaction will be in equilibrium.

This is an attempt to determine which surface reactions are important in potential regimes used in this study. Obviously, it is impossible to identify all the reactions which may occur since this is a complicated system. The reactions involving chromium, nickel, and iron are only considered here with the effect of trace elements neglected. Also, it is assumed that the reactions involving each of the major alloy components occur more or less independently.

The basic approach used here assumes that an oxide surface layer is broken down in several stages to form hydroxide or chloride complexes.

For experiments done in this study, the electrochemical breakdown of the passive film is unlikely. On the average, the equilibrium potential for the oxide reactions is approximately 200mV SHE ($\sim$ 1800mV SCE). More likely processes for premature

passive film breakdown are: a) mechanical breakdown of the passive film, b) chloride adsorption to change the conductivity properties of the film, or c) preferential dissolution of certain precipitates such as sulfides.

After localized breakdown of the passive film occurs, accelerated dissolution at these small relatively anodic areas leads to pitting. Rapid dissolution prevents the surface from reforming the passive film. Consequently, the active base metal is exposed to the environment. This discussion assumes that this active surface may then be oxidized to form chloride complexes.

Standard oxidation potentials are used with the Nernst equation* to calculate the equilibrium potential for a given chloride formation. The oxidation potentials and reaction constants used here were obtained from several sources and reflect the more recent or accepted values as much as possible (58,59). Uncertainties in the experimental values determined for the reaction constants allow one to merely approximate the equilibrium potentials for the chloride formations.

The reader should be cautioned that these reactions are not standard redox reactions but are written to reflect the physical situation. For example, chloride reduction is not considered.

* The Nernst equation is given by:

$$E = E^\circ + \frac{RT}{ZF} \ln K$$

Where E° = Standard oxidation potential

R = Universal gas constant

Z = Valence transfer

F = Faraday constant

K = Stability or reaction constant

For T = 298° K, the equation becomes

$$E = E^\circ + \frac{0.0592}{Z} \log K \text{ (volts)}$$

---

although in certain circumstances it may occur.

On the active surface, obtained during the pitting process, chromium is oxidized:

$$Cr(s) = Cr^{+2} + 2e^- \qquad E^\circ = 557mV \text{ SHE}$$

$$Cr^{+2} = Cr^{+3} + e^- \qquad E^\circ = 410mV \text{ SHE}$$

Or by the direct process:

$$Cr(s) = Cr^{+2} + 2e^- \qquad E^\circ = 740mV \text{ SHE}$$

As a result of either the passive film breakdown or active surface oxidation, the chromium chloride formation can be described by the following:

$$Cr^{+3} + Cl^- = CrCl^{+2} \qquad \log K_1 = 0.60 \quad E = 752mV \text{ SHE}$$

and

$$Cr^{+3} + 2Cl^{-} = CrCl_2^{+} \quad \log K_2 = -0.71 \quad E° = 726mV\ SHE$$

As with chromium, oxidizing active nickel during pitting gives the following:

$$Ni(s) = Ni^{+2} + 2e^{-} \quad E° = 250mV\ SHE$$

The oxidized nickel may then form a chloride by the reaction:

$$Ni^{+2} + Cl^{-} = NiCl^{+} \quad \log K = 0.89 \quad E° = 276mV\ SHE$$

by the Nernst equation.

Active iron during pitting may be oxidized in stages by the following:

$$Fe(s) = Fe^{+2} + 2e^{-} \quad E° = 440mV\ SHE$$

and

$$Fe^{+2} = Fe^{+3} + e^{-} \quad E° = -770mV\ SHE$$

or by the direct process:

$$Fe(s) = Fe^{+3} + 3e^{-} \quad E° = 36mV\ SHE$$

The iron chloride may then be formed:

$$Fe^{+3} + Cl^{-} = FeCl^{+2} \quad \log K = 1.48 \quad E° = 66mV\ SHE$$

In addition to the simple chloride, an iron perchlorate may be formed as described by the following reaction:

$$Fe^{+3} + 3(ClO_4^{-}) = Fe(ClO_4)_3 \quad \log K = 1.15 \quad E° = 59mV\ SHE$$

by the Nernst equation. The perchlorate formation is pH inde-

pendent as seen from the reaction and may proceed if the chloride ion can actually enter the oxide film and form the perchlorate radical.

The results for the complex formations are summarized in Figure 32. Since the stability constant is defined as the proper product of the activities of the products divided by the proper product of the activities of the reactants, and the oxidation potential is constant, increasing the applied potential in the noble direction implies the stability of the products from the Nernst equation. The potentials for complex formations identified earlier are equilibrium potentials. At potentials more noble than the equilibrium potential, a given complex should be stable.

BIBLIOGRAPHY

1. Hoar, T.P., Corrosion, Vol. 19, 1963, pp. 331.

2. Hodge, J.C. and Miller, J.L., Trans. Amer. Soc. Metals, Vol. 28, 1940, pp. 25.

3. Pugh, E.N. Green, A.A.S., and Sedriks, A.J., Interface Conference, Australian Inst. of Metals, Melbourne, 1969, pp. 237.

4. Staehle, R.W., Stress Corrosion Cracking of the Fe-Cr-Ni Alloy System, Proceedings NATO Conference, Brussels, 1970.

5. Latanision, R.M. and Staehle, R.W., Fundamental Aspects of Stress Corrosion Cracking, Eds., Staehle, R.W., Forty, A.J., Van Rooyen, D., National Association of Corrosion Engineers, Houston, 1969, pp. 214.

6. Kinzell, A.B., Journal of Metals, Vol. 4, 1952, pp. 469.

7. Wranglen, G., Corrosion Science, Vol. 14, 1974, pp. 331.

8. Smialowski, M., Szklarska-Smialowska, Z., Rychik, M., and Szummer, A., Corrosion Science, Vol. 9, 1969, pp. 123.

9. Joshi, A. and Stein, D.F., Corrosion, Vol. 28, 1972, pp. 321.

10. Barnartt, S., Corrosion, Vol. 18, 1962, pp. 322.

11. Rosenfeld, I.L., and Danilov, I.S., Corrosion Science, Vol. 7, 1967, pp. 129.

12. Thomas, K.C., Stickler, R., and Allio, R.J., Corrosion Science, Vol. 5, 1965, pp. 71.

13. Scully, J.C., Corrosion Science, Vol. 7, 1967, pp. 197.

14. Scully, J.C., Corrosion Science, Vol. 8, 1968, pp. 513.

15. Molotskii, M.I., Kinetika J. Kataliz, Vol. 13, 1972, pp. 898.

16. Uhlig, H., Physical Metallurgy of Stress Corrosion Fracture, Ed. Rhodin, T., Interscience, New York, 1959, pp. 1.

17. Greene, N.D., and Fontanta, M.G., Corrosion, Vol. 15, 1959, pp. 41.

18. Kolotyrkin, J.M., Corrosion, Vol. 19, 1963, pp. 261.

19. Szlarska-Smialowska, Z., Corrosion, Vol. 27, 1971, pp. 223.

20. Vetter, K.J. and Strehblow, H.H., Zeitschrift "Fur Electrochemie, Vol. 74, 1960, pp. 449.

21. Vetter, K.J. and Strehblow, H.H., Zeitschrift "Fur Electrochemie, Vol. 74, 1970, pp. 1025.

22. Vetter, K.J. and Strehblow, H.H., Localized Corrosion, NACE - 3, 1974, pp. 240.

23. Strehblow, H.H., and Wenners, J. Zeitschrift "Fur Phys. Chem., Vol. 98, 1975, pp. 199.

24. Rideout, S.P., and Undrejcin, R.S., and Louthan, M.R., The Science, Technology and Application of Titanium, Ed. Jaffee, R.I., and Promisel, N.E., Pergamon Press, 1968, pp. 307.

25. Vermilyear, D.A. and Diegle, R.B., Corrosion, Vol. 32, 1976, pp. 26.

26. Edeleanu, C., J. of Iron & Steel Inst., Vol. 173, 1953, pp. 140.

27. Vaccaro, F., M.S. Thesis, Case Western Reserve University, 1977.

28. Nielson, N.A., Journal of Materials, Vol. 5, 1970, pp. 794.

29. Boyd, W.K. and Vaughn, D.A., Society of Manufacturing Engineers, IQ 73-624, 1973.

30. Gest, R.J. and Troiano, A.R., "L' Hydrogene Dans Les Metaux", Edinong Science et Industrie, Paris, 1972, pp. 427.

31. Papp, J., Hehemann, R.F., and Troiano, A.R., Hydrogen in Metals, Proceedings ASM Conference, Seven Springs, Pa., 1973, pp. 657.

32. Whiteman, M.B. and Troiano, A.R., Corrosion, Vol. 21, 1965, pp. 125.

33. Troiano, A.R., Hehemann, R.F., and Shively, J.H., Colloque Sur L'Hydrogene Dans Les Metaux, Valduc, 1967, pp. 109.

34. Papp, J., M.S. Thesis, Case Western Reserve University, 1973.

35. Ro, H.K., M.S. Thesis, Case Western Reserve University, 1974.

36. Ateya, B.G. and Pickering, H.W., Hydrogen in Metals, Proceedings ASM Conference, Seven Springs, Pa., 1973, pp. 207.

37. Van leeuwen, H.P., Corrosion, Vol. 32, 1976, pp. 34.

38. Oriani, R.A., Actamet., Vol. 22, 1974, pp. 1065.

39. Oriani, R.A., Int. Conference on Stress Corrosion Cracking and Hydrogen Embrittlement of Iron Based Alloys, 42 Unieux-Firminy, France, June 1973.

40. Benninghoven, Applied Physics, Vol. 1, 1973, pp. 3.

41. Liebl, H.J., J. of App. Phys., Vol. 38, 1967, pp. 5277.

42. Liebl, H.J., and Herzog, R.F.K., J. of App. Physc., Vol. 32, 1961, pp. 1197.

43. Barrington, A.E. Herzog, R.F.K., and Poschenrieder, W.P., "The Ion Microprobe Mass Spectrometer", Progress in Nuclear Energy, Series IX, Vol. 7, Pergamon Press, New York, 1966.

44. Barrington, A.E., Herzog, F.F.K., and Poschenrieder, P., Journal of Vac. Sci. & Tech., Vol. 3, 1966, pp. 239.

45. Herzog, R.F.K., Poschenrieder, W.P., and Satkiewicz, F.G., NASA CR-683, Goddard Space Flight Center, 1967.

46. Herzog, R.F.K., "The Transmission of Ions Through Double Focusing Mass Spectrometers", Trace Analysis By Mass Spectrometry, Academic Press, 1972, pp. 57.

47. Heimerl, G.J. and Braski, D.N., Materials Research And Standards, January 1965, pp. 18.

48. Truhan, J. and Hehemann, R.F., Nasa Contractor Report CR-134711, Lewis Research Center, 1974.

49. deErceville, O., M.S. Thesis, Case Western Reserve University, 1975.

50. Okamoto, G., Corrosion Science, Vol. 13, 1973, pp. 471.

51. Greene, N.D., Corrosion, Vol. 18, 1962, pp. 136.

52. Greene, N.D., and Fontana, M.G., Corrosion, Vol. 13, 1959, pp. 39.

53. ASTM Designation G5-72, 1972, pp. 525.

54. Gerasimov, V.V., Shuvalov, V.A. and Andreeva, S.A., Zashchita Metallov, Vol. 8, 1972, pp. 450.

55. Smith, T., J. Electrochem Soc.: Solid State Science and Technology, Vol. 119, 1972, pp. 1398.

56. Herzog, R.F.K., Personal Communications.

57. Nielsen, N.A., Int. Conference on Stress Corrosion Cracking and Hydrogen Embrittlement of Iron Based Alloys, 42 Unieux-Firminy, France, June 1973.

58. Stability Constants of Metal-Ion Complexes, Eds. Sillen, L.G., and Martell, A.E., London Chemical Society Special Publication 17, London, 1964.

59. Handbook of Chemistry and Physics, 54th Ed., Ed. by Weast, R.C., CRC Press, Cleveland, 1973.

TABLES

ELEMENT	WEIGHT PERCENT
Chromium	24.15
Nickel	19.45
Iron	Balance
Silicon	0.38
Phosphorus	0.018
Sulfur	0.001
Manganese	1.41
Carbon	0.054
Tensile Strength = 40,100 psi	
Ultimate Yield Strength = 37,400 psi	

TABLE 1

COMPOSITION OF TYPE 310 STAINLESS STEEL
AND RELATED TENSILE DATA

PRIMARY BEAM COMPOSITION	ARGON
Primary Accelerating Voltage	10 kV
Sputter Area	6.3 mm^2
Target Current Density	5 $\mu A/mm^2$
Secondary Accelerating Voltage	$\pm$ 1 kV
Detector Voltage	3 kV
Pressure-Sample Chamber (Without Beam)	2 x 10^{-7} torr
Pressure-Sample Chamber (With Beam)	2 x 10^{-6} torr
Pressure-Mass Spectrometer	1 x 10^{-7} torr

TABLE 2

IMPORTANT SIMS INSTRUMENT PARAMETERS

SPECIES	NORMALIZED INTENSITY
H^+	0.094-0.140
O^-	0.014-0.080
OH^-	0.012-0.025
Na^+	0.110
Mg^+	0.019
Cl^-	0.077
Cr^+	3.48
Ni^+	0.10

TABLE 3

BACKGROUND LEVELS FOR A NOMINALLY CLEAN UNPOLARIZED SPECIMEN OF 310 STAINLESS STEEL

SPECIES	NORMALIZED INTENSITY
H^+	7.09
O^-	0.72
OH^-	0.21
Mg^+	2.91
Cl^-	1.82
Cr^+	3.18
Ni^+	4.55

TABLE 4

SIMS ANALYSIS OF A PRIMARY STRESS CORROSION CRACKED FRACTURE SURFACE

FIGURES

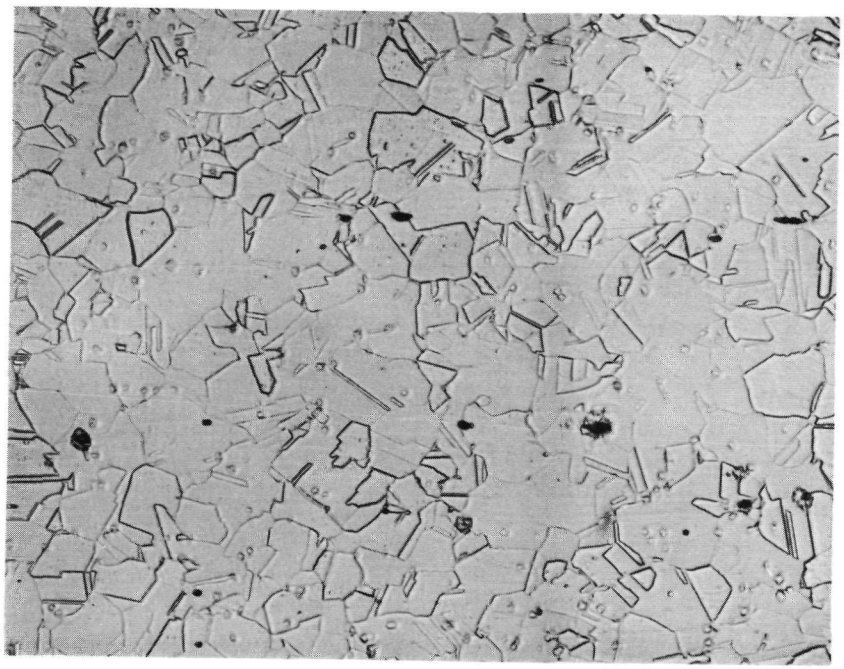

FIGURE 1: LIGHT METALLOGRAPHY OF THE AS-RECEIVED SURFACE OF TYPE 310 STAINLESS STEEL, 250X.

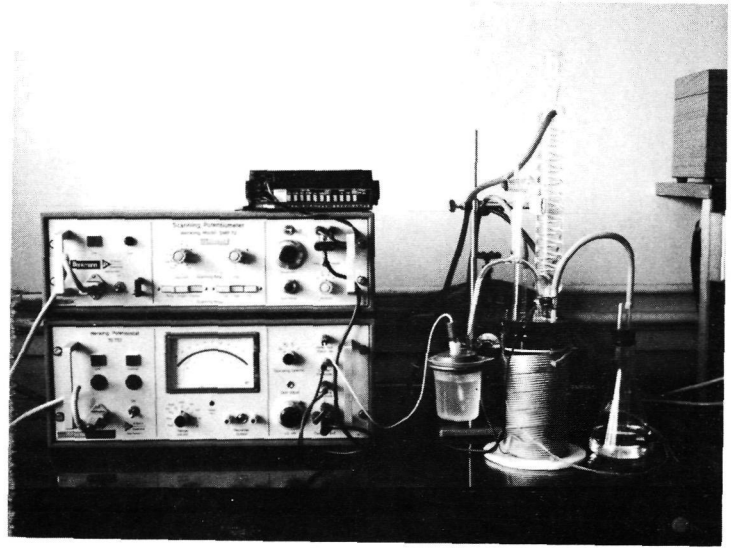

FIGURE 2: ELECTROCHEMICAL TEST CELL AND ASSOCIATED ELECTRONICS.

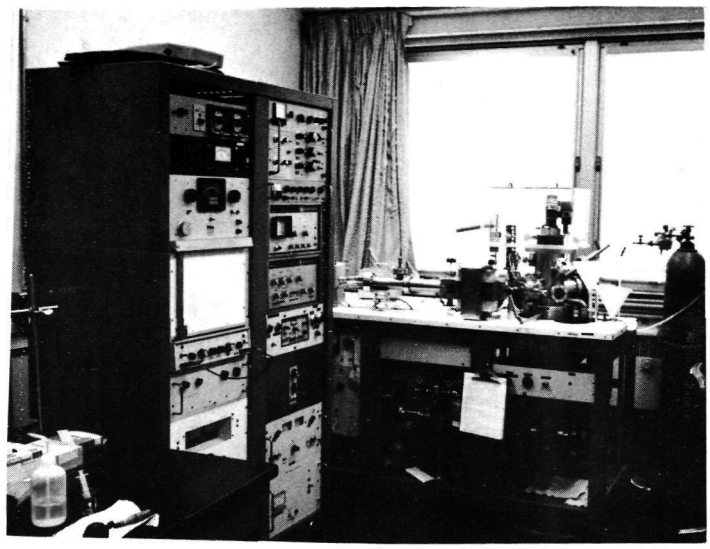

FIGURE 3: SIMS AND THE ASSOCIATED ELECTRONICS.

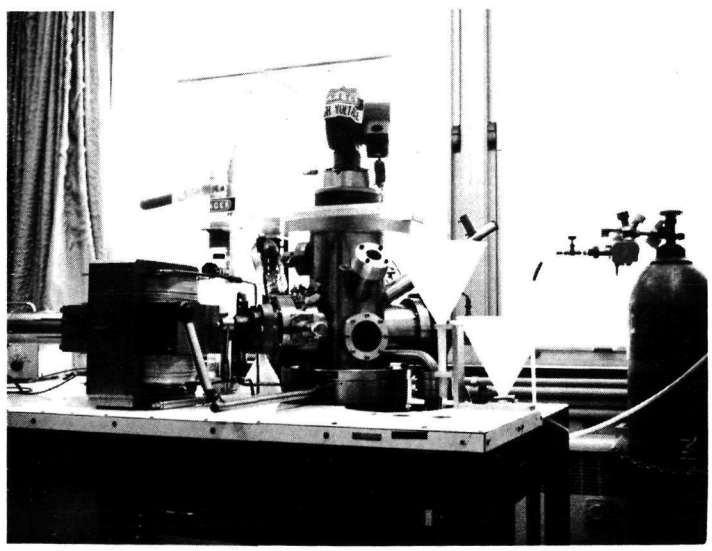

FIGURE 4: DETAIL OF SIMS SHOWING SAMPLE CHAMBER AND MASS SPECTROMETER.

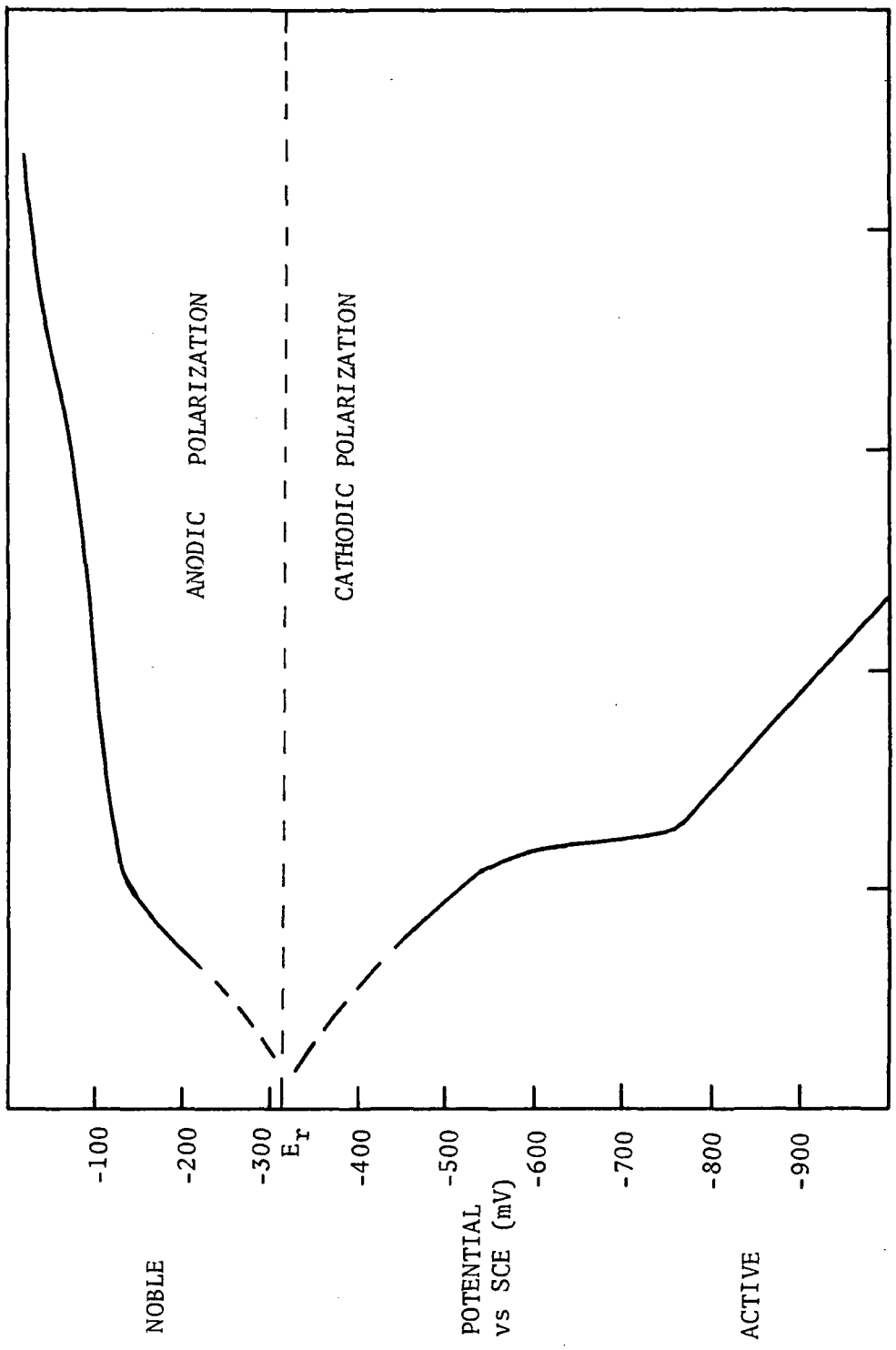

FIGURE 5: POLARIZATION CURVE FOR 310 STAINLESS STEEL IN 5M NaCl, DEAERATED AT 23°C.

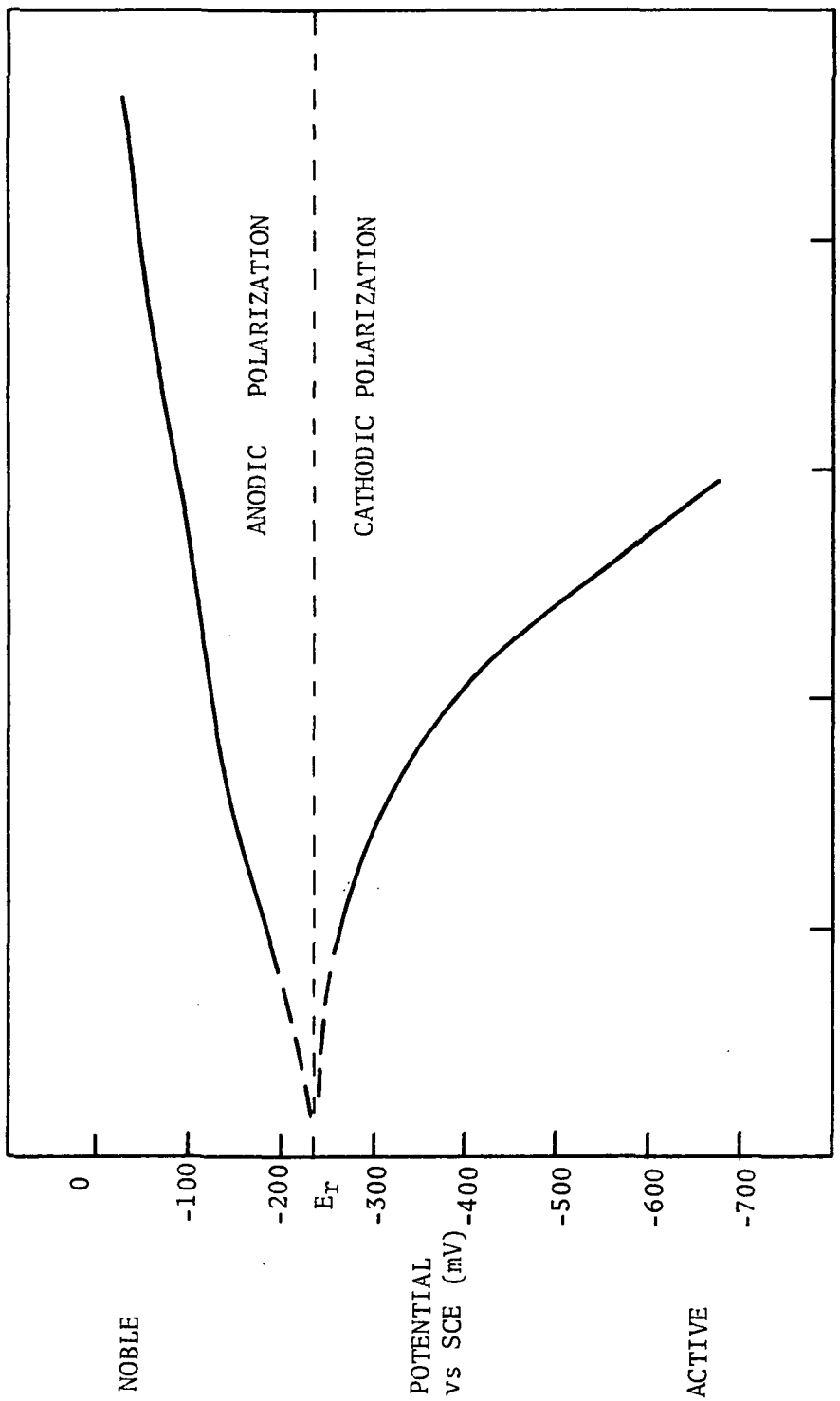

FIGURE 6: POLARIZATION CURVE FOR 310 STAINLESS STEEL IN 5M NaCl, AERATED AT 23°C.

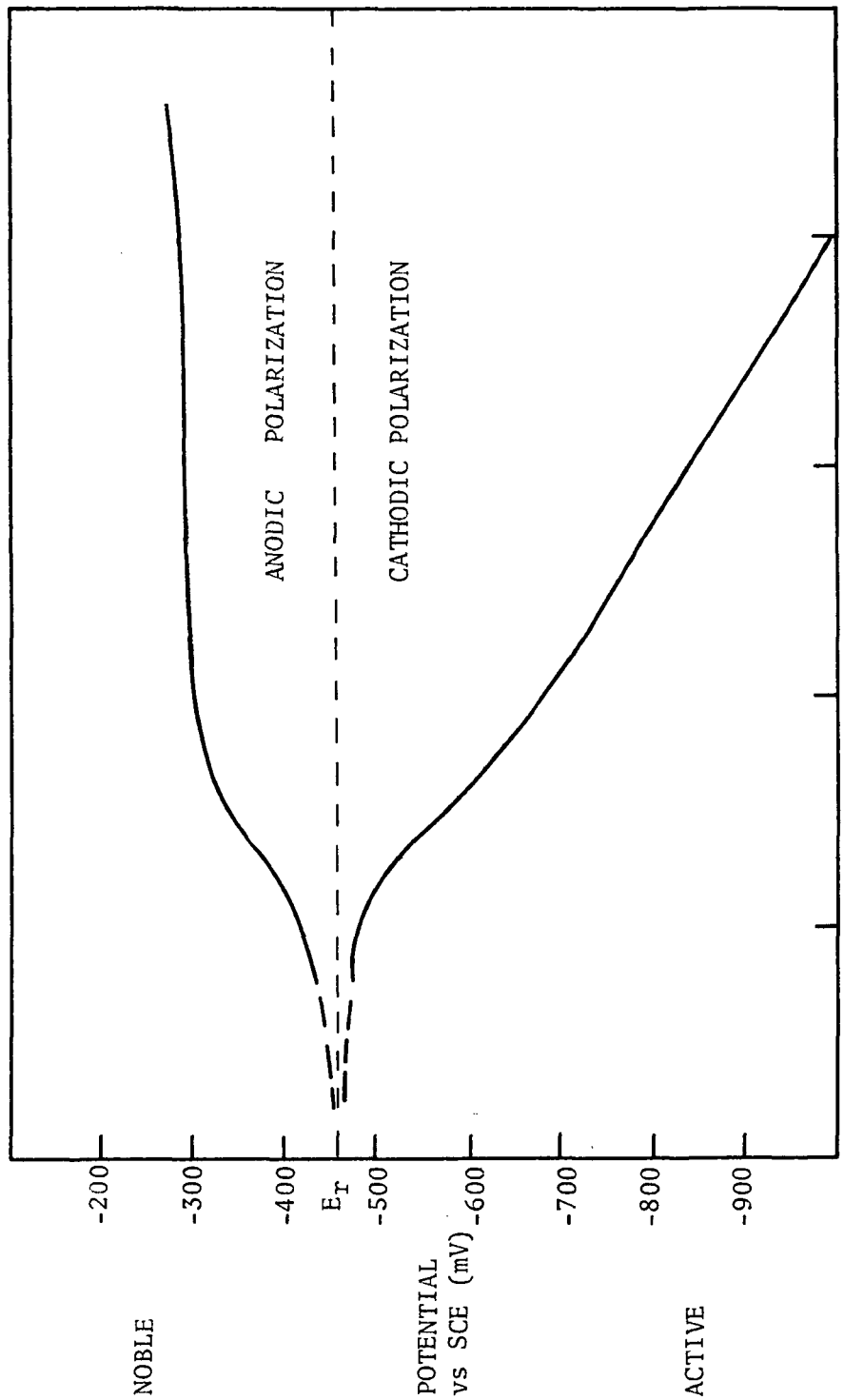

FIGURE 7: POLARIZATION CURVE FOR 310 STAINLESS STEEL IN 5M NaCl, DEAERATED AT 105°C.

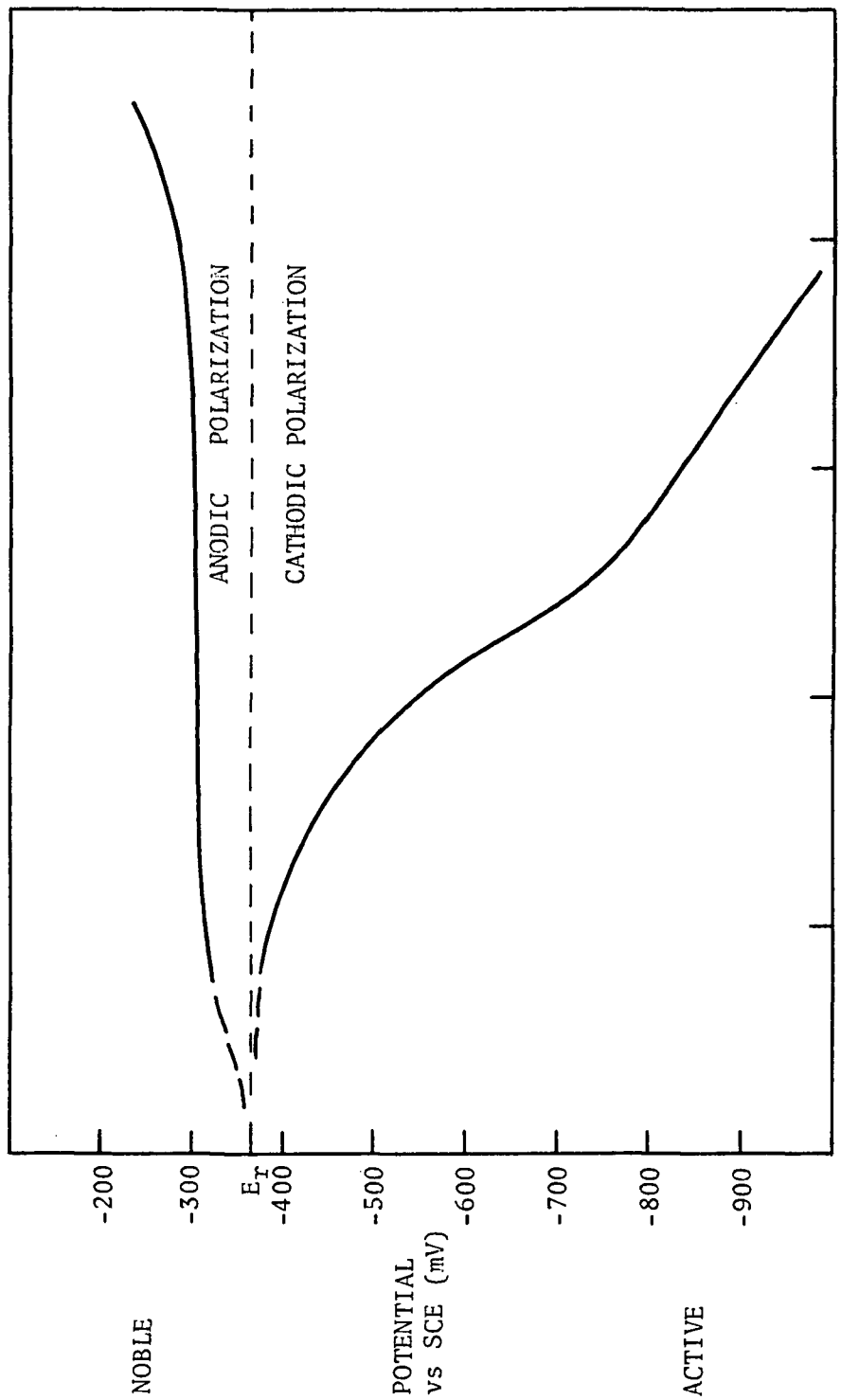

FIGURE 8: POLARIZATION CURVE FOR 310 STAINLESS STEEL IN 5M NaCl, AERATED AT 105°C.

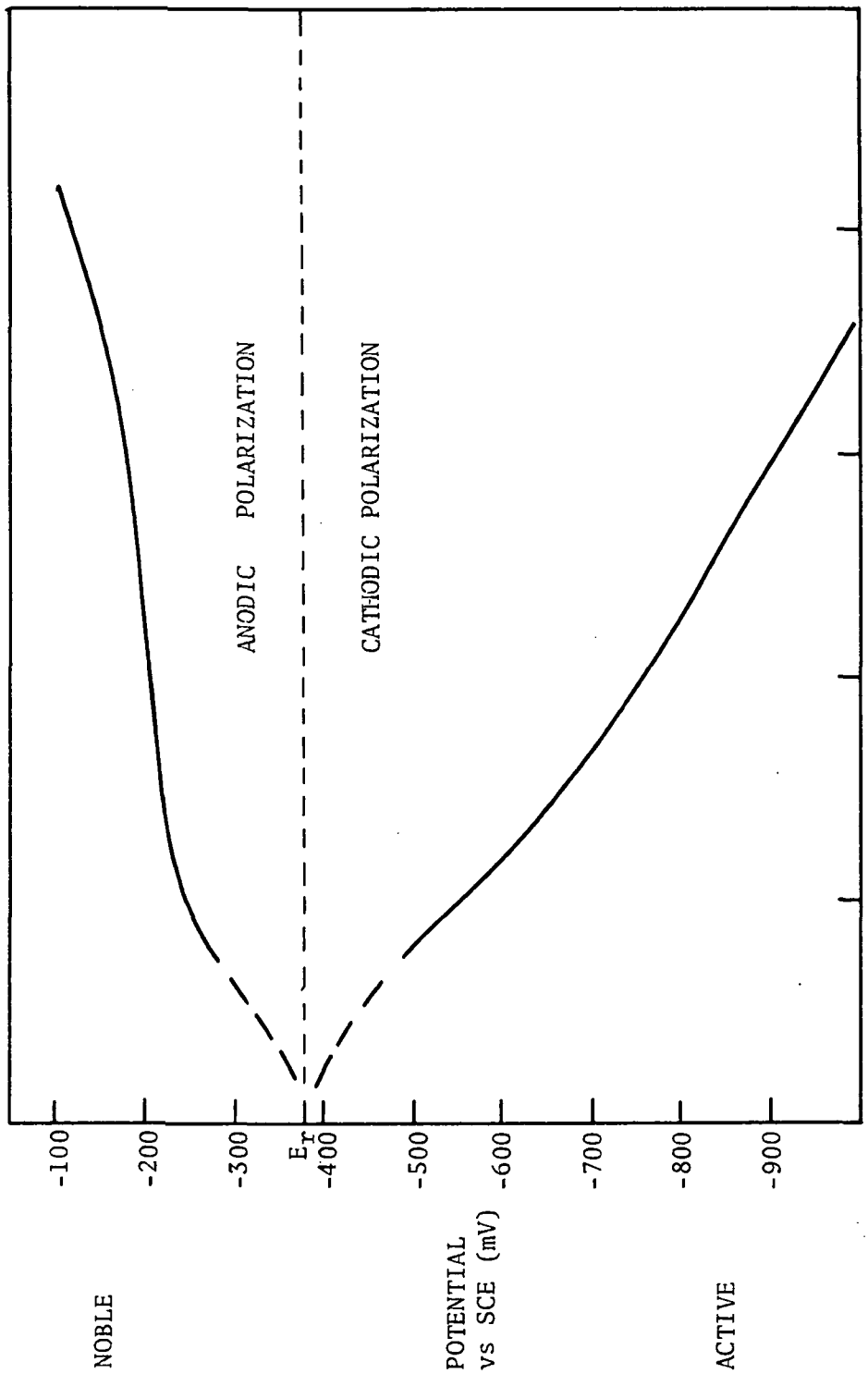

FIGURE 9: POLARIZATION CURVE FOR 310 STAINLESS STEEL IN 2.5M $MgCl_2$, DEAERATED AT 23°C.

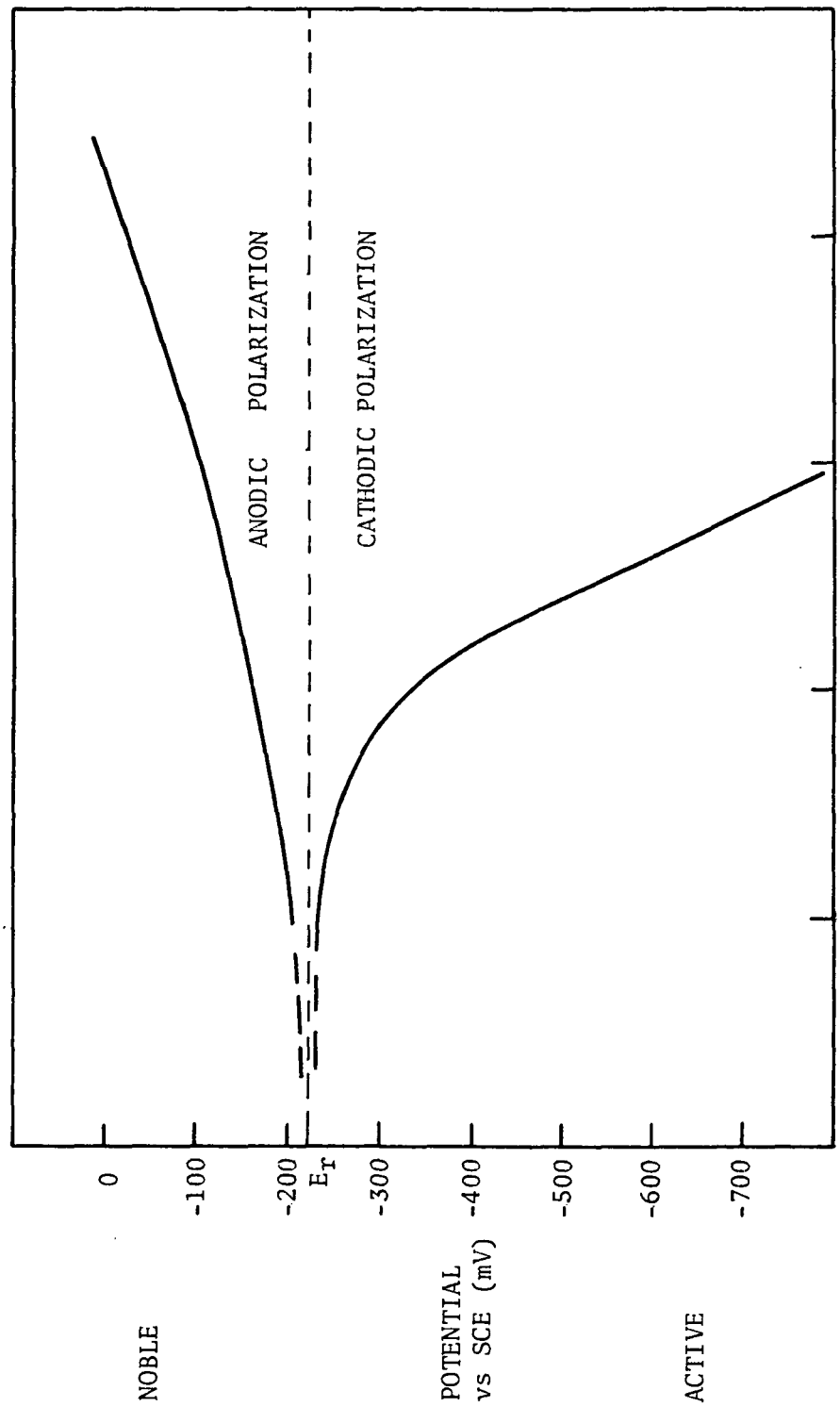

FIGURE 10: POLARIZATION CURVE FOR 310 STAINLESS STEEL IN 2.5M $MgCl_2$, AERATED AT 23°C.

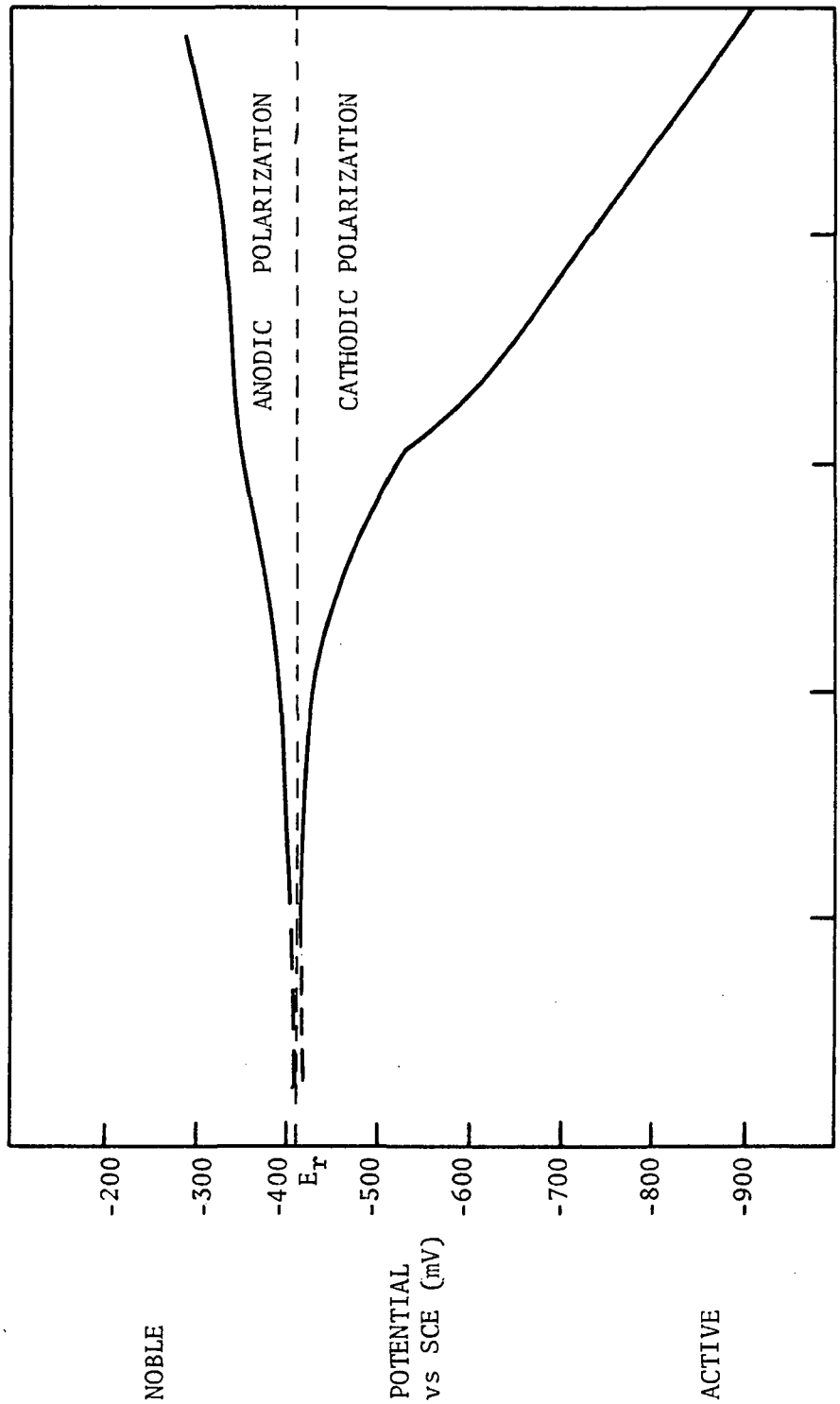

FIGURE 11: POLARIZATION CURVE FOR 310 STAINLESS STEEL IN 2.5M $MgCl_2$, DEAERATED AT 108°C.

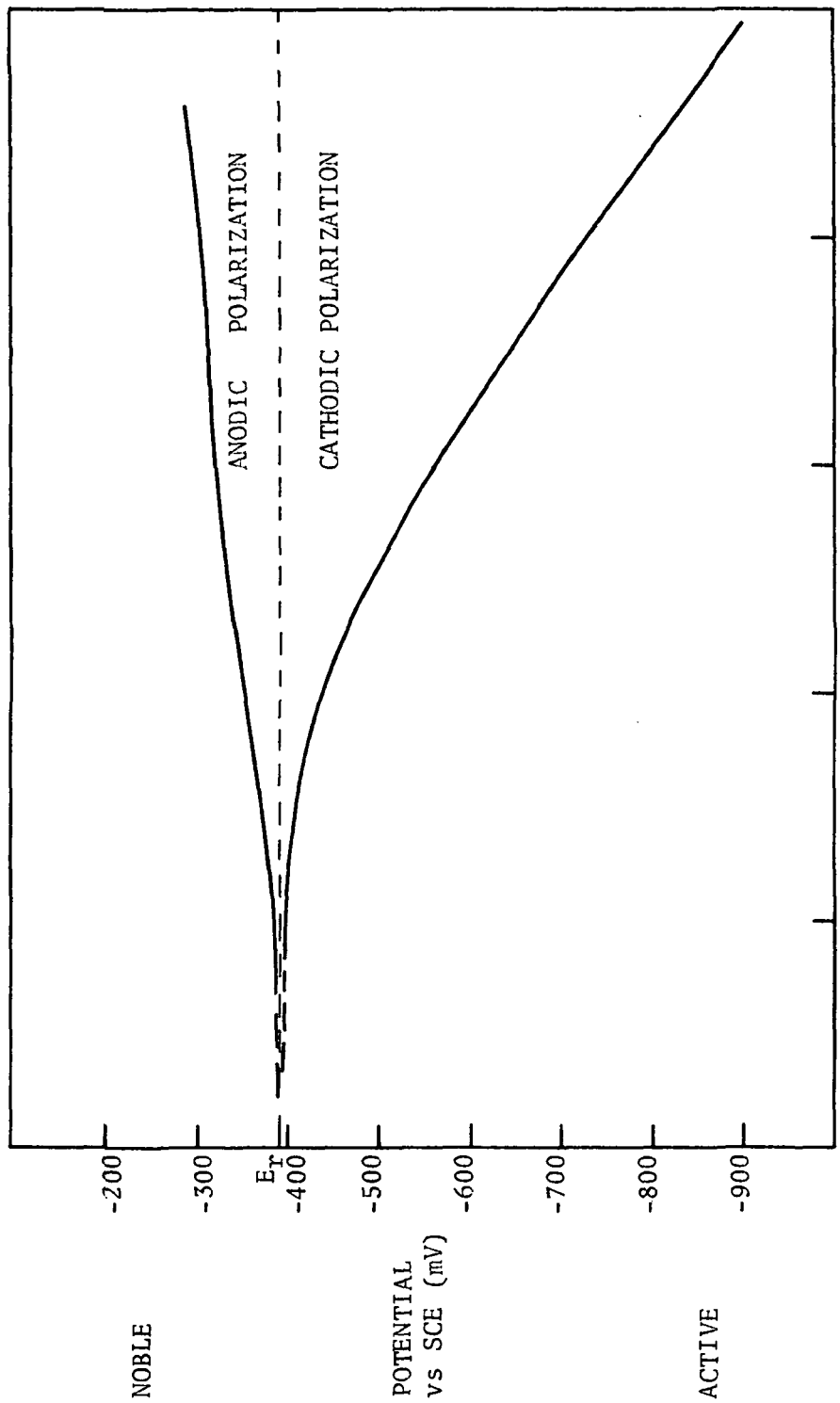

FIGURE 12: POLARIZATION CURVE FOR 310 STAINLESS STEEL IN 2.5M $MgCl_2$, AERATED AT 108°C.

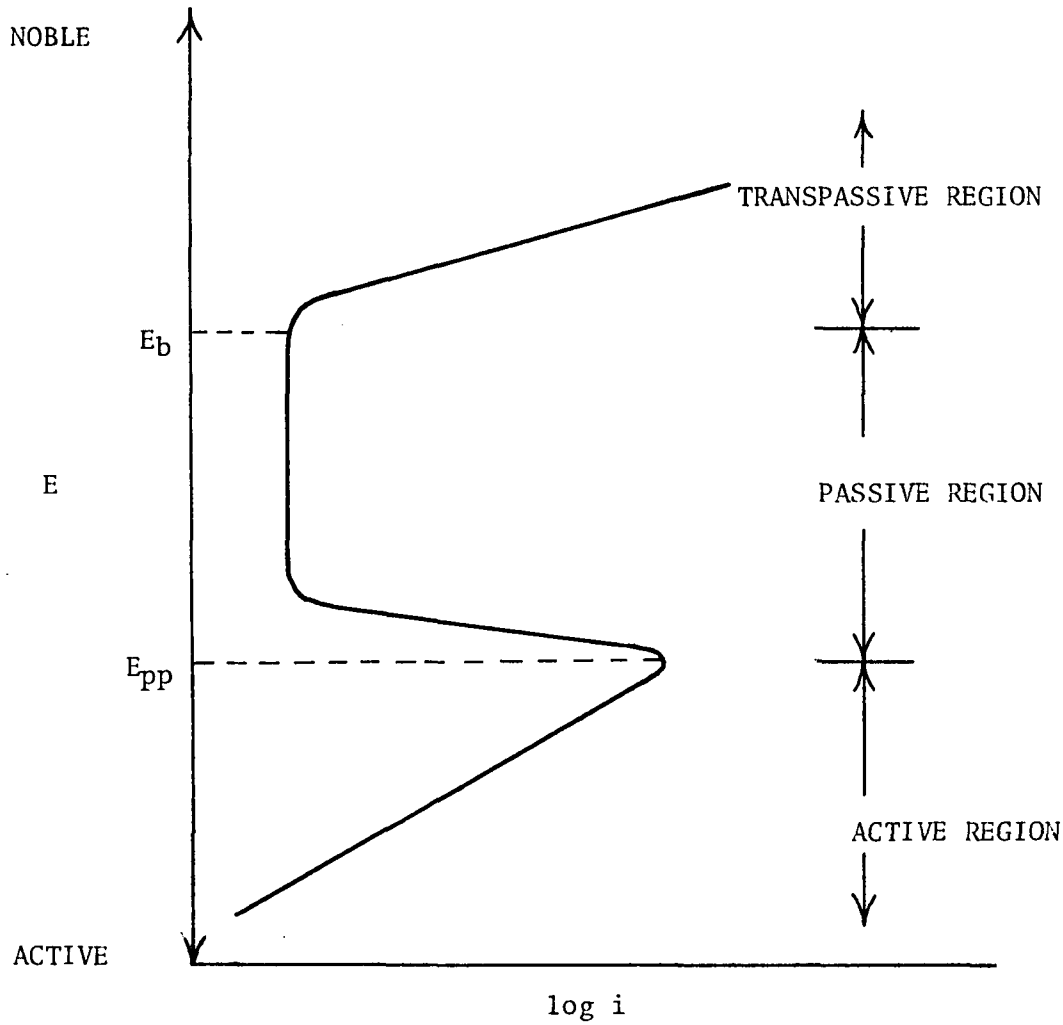

FIGURE 13a: IDEAL METAL OXIDATION REACTION SHOWING ACTIVE PASSIVE BEHAVIOR.

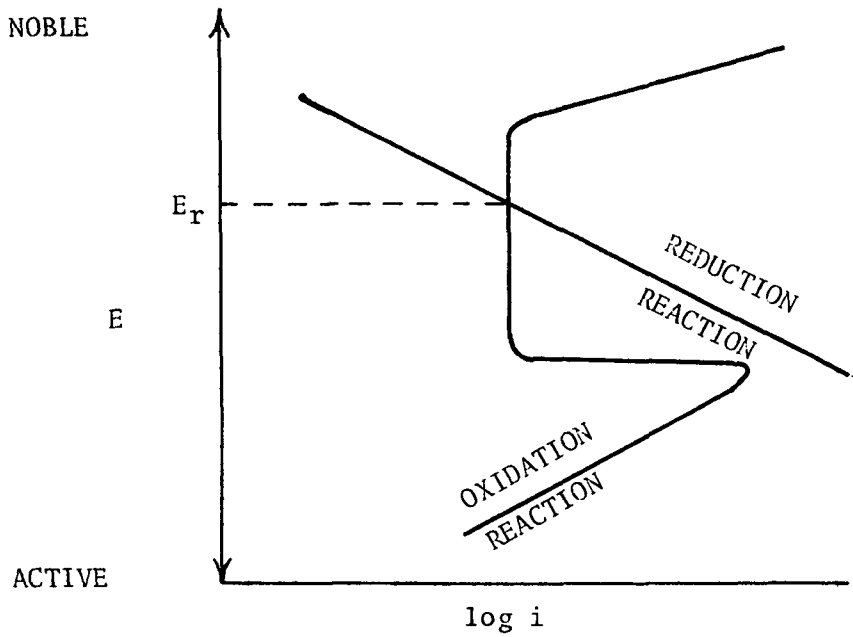

FIGURE 13b: REDUCTION REACTION SUPERIMPOSED ON THE METAL OXIDATION REACTION.

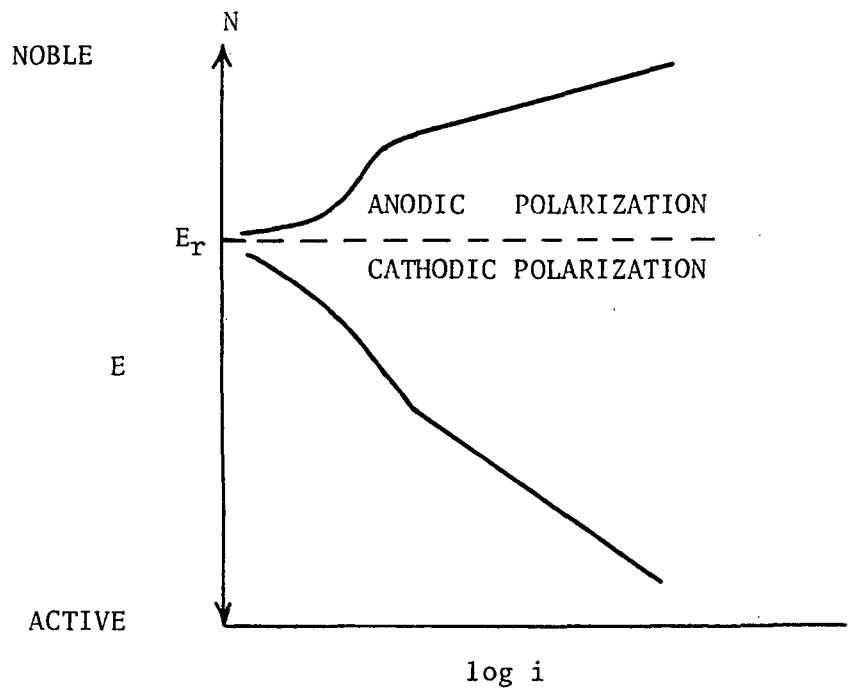

FIGURE 13c: RESULTANT POLARIZATION CURVE MEASURED EXPERIMENTALLY.

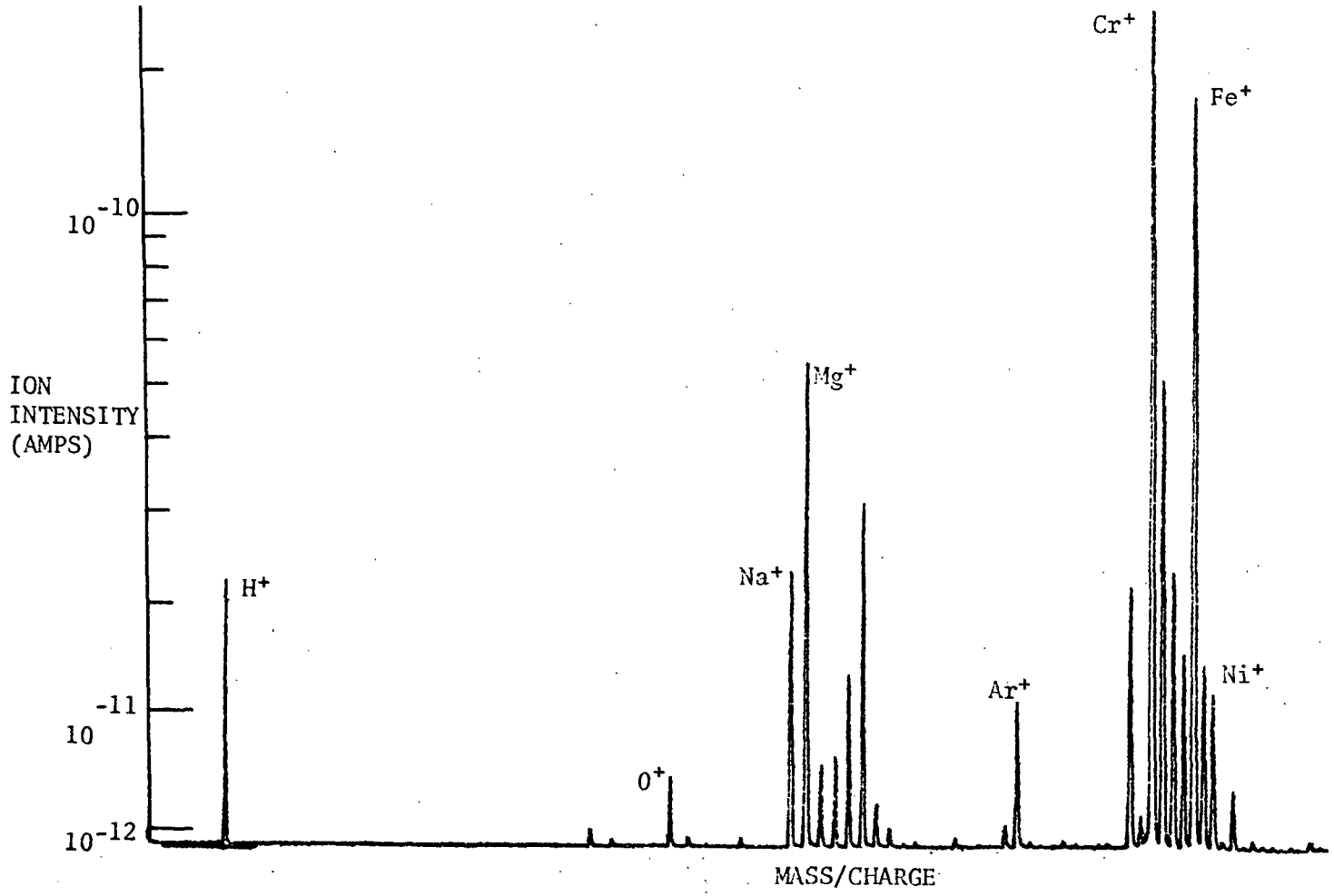

FIGURE 14: MASS SPECTRUM OF THE POSITIVE IONS SHOWING THE MAJOR ALLOY COMPONENTS AFTER ANODIC POLARIZATION IN $MgCl_2$.

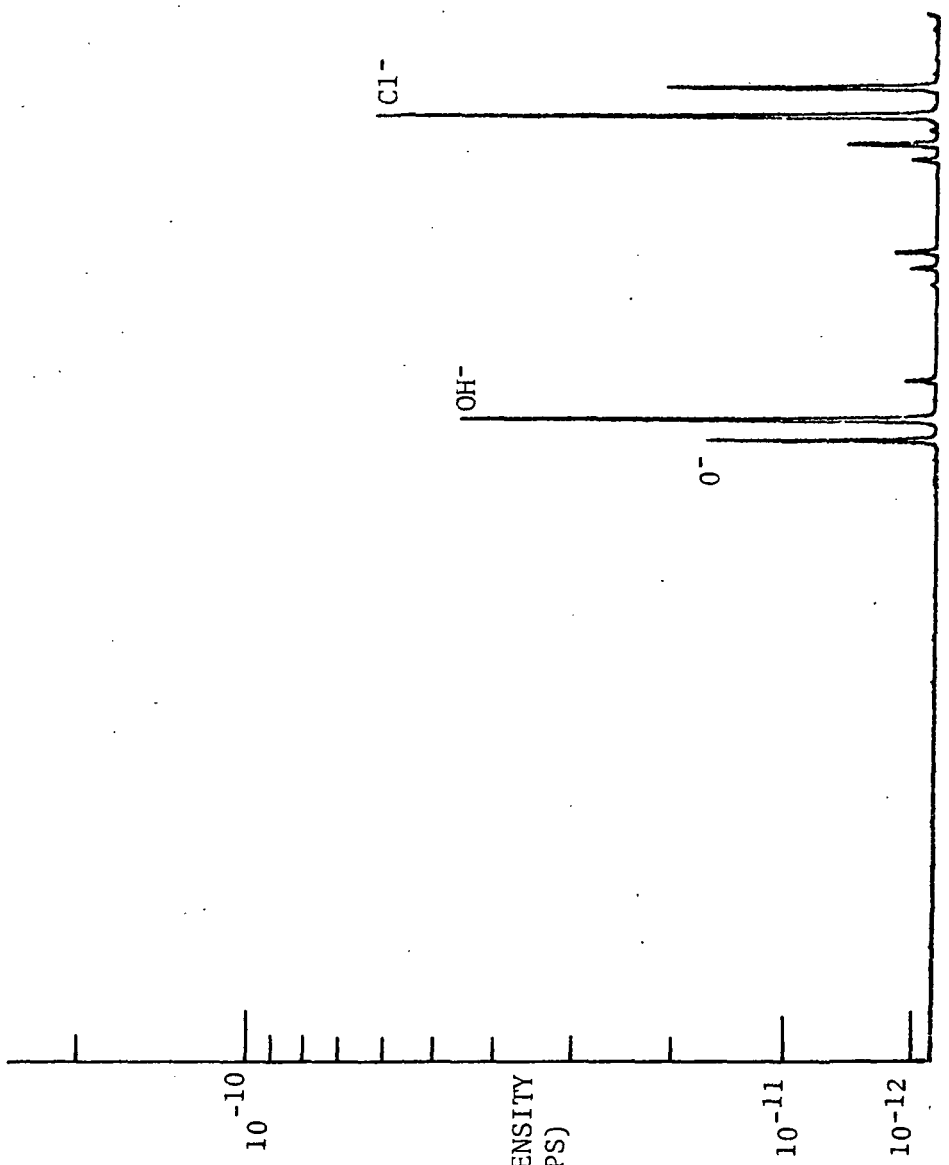

FIGURE 15: MASS SPECTRUM OF THE NEGATIVE IONS AFTER ANODIC POLARIZATION IN $MgCl_2$.

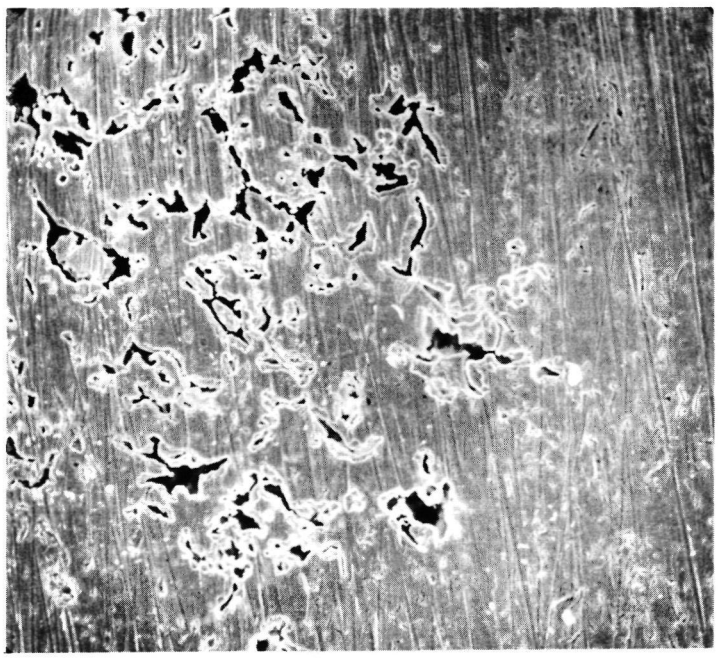

FIGURE 16: PITTED SURFACE OF 310 STAINLESS STEEL AFTER ANODIC POLARIZATION IN 5M NaCl, 23°C, 300X.

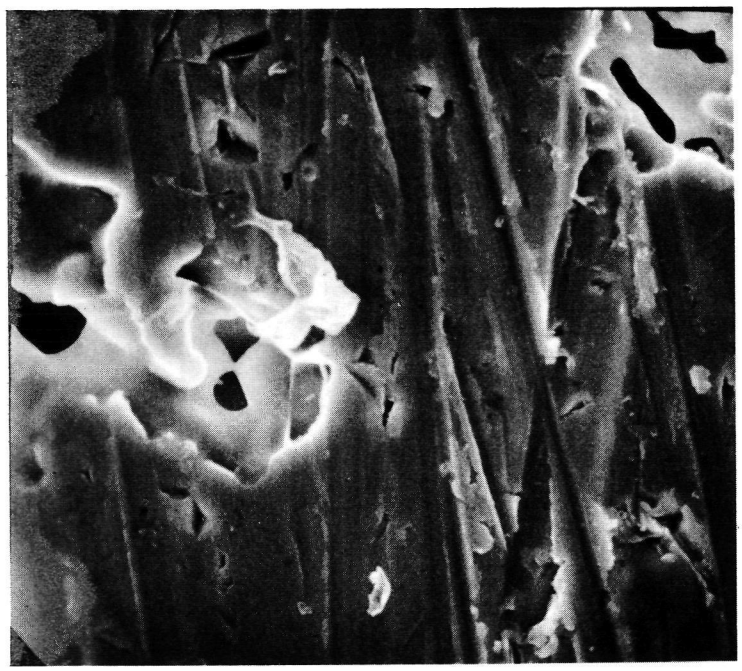

FIGURE 17: DETAIL OF THE PITTED SURFACE OF 310 STAINLESS STEEL AFTER ANODIC POLARIZATION IN 5M NaCl, 23°C, 3000X.

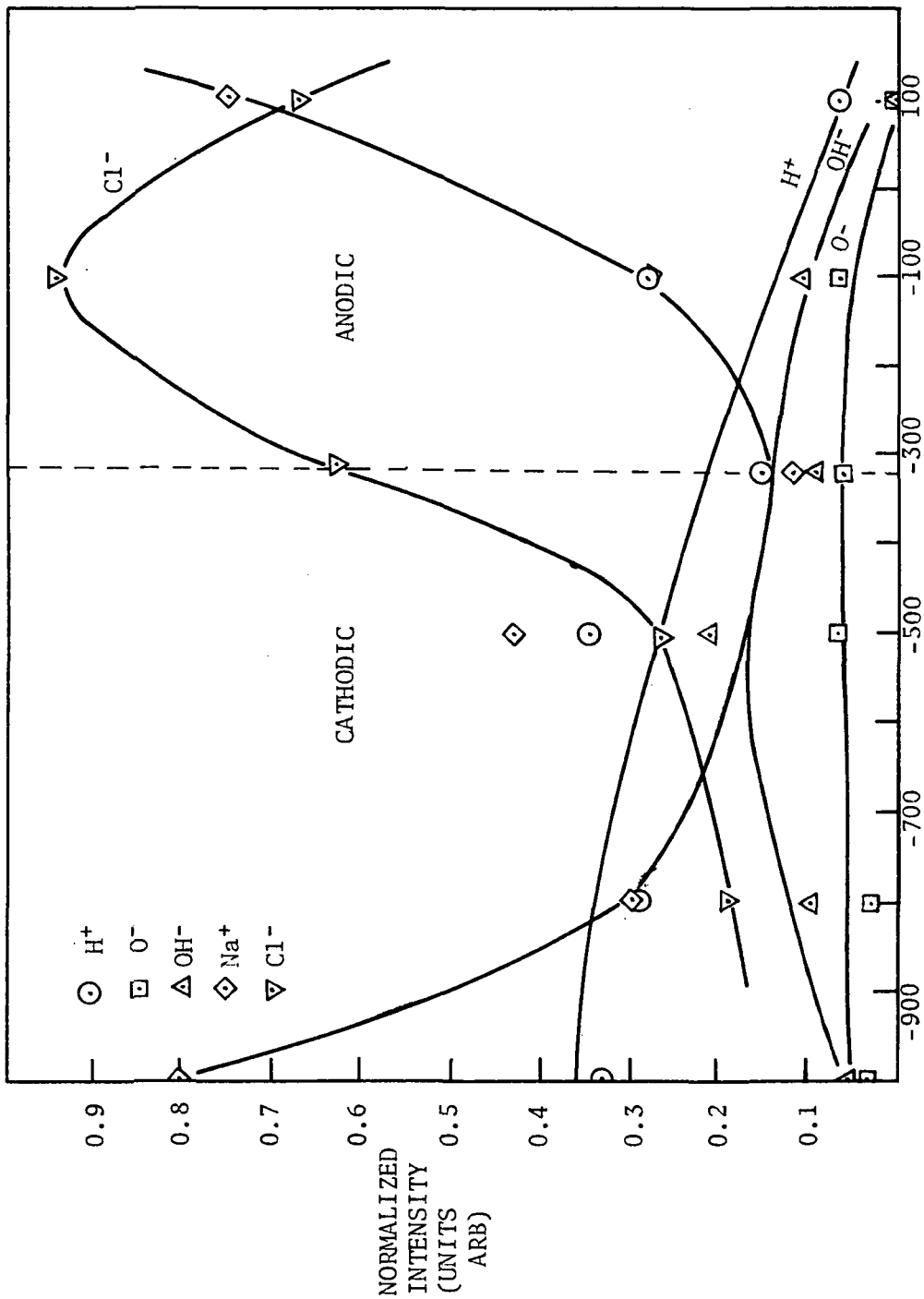

FIGURE 18a: CONCENTRATION VS POTENTIAL FOR 310 STAINLESS STEEL IN 5M NaCl, DEAERATED AT 23°C.

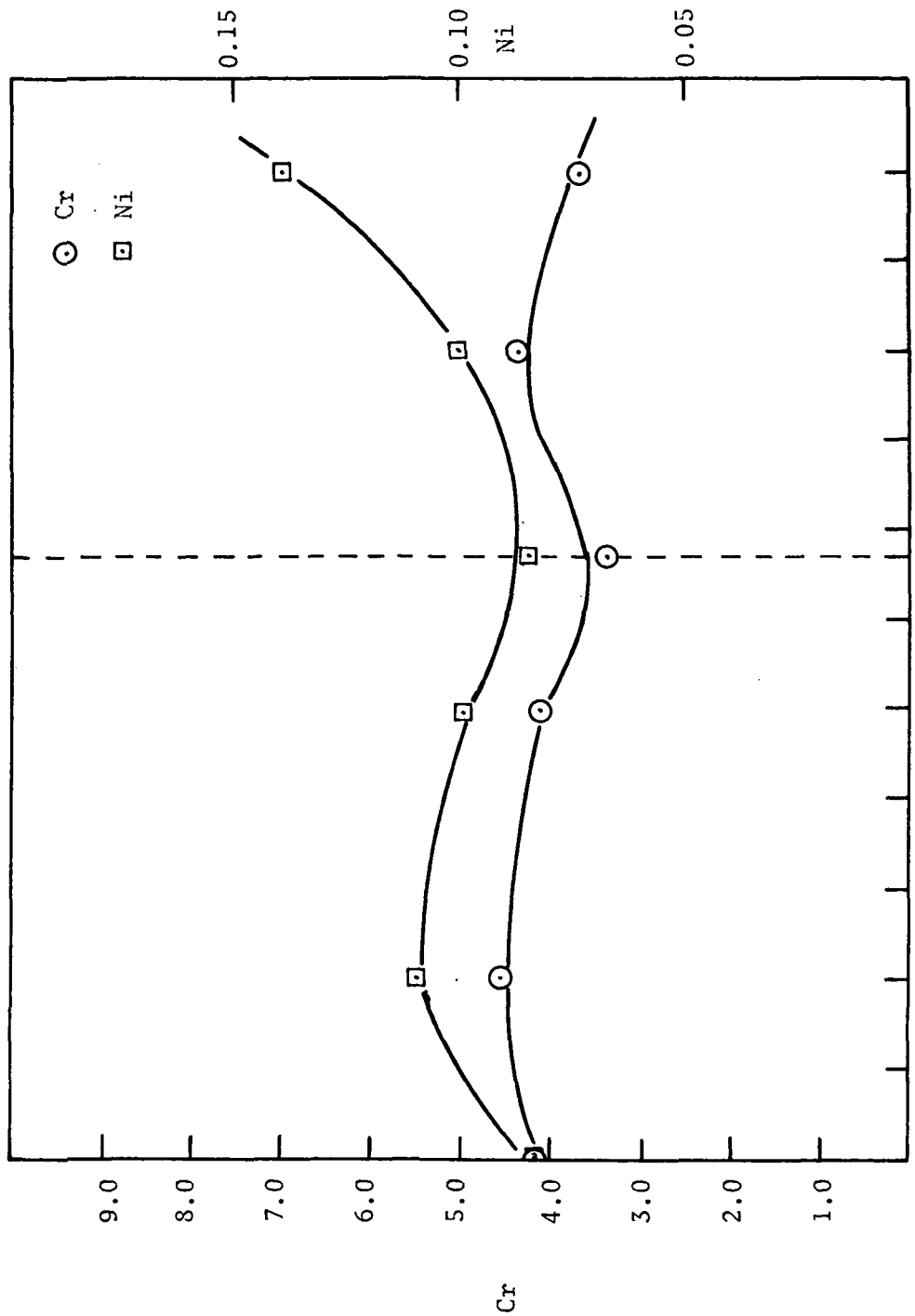

FIGURE 18b: CONCENTRATION VS POTENTIAL FOR 310 STAINLESS STEEL IN 5M NaCl, DEAERATED AT 23°C.

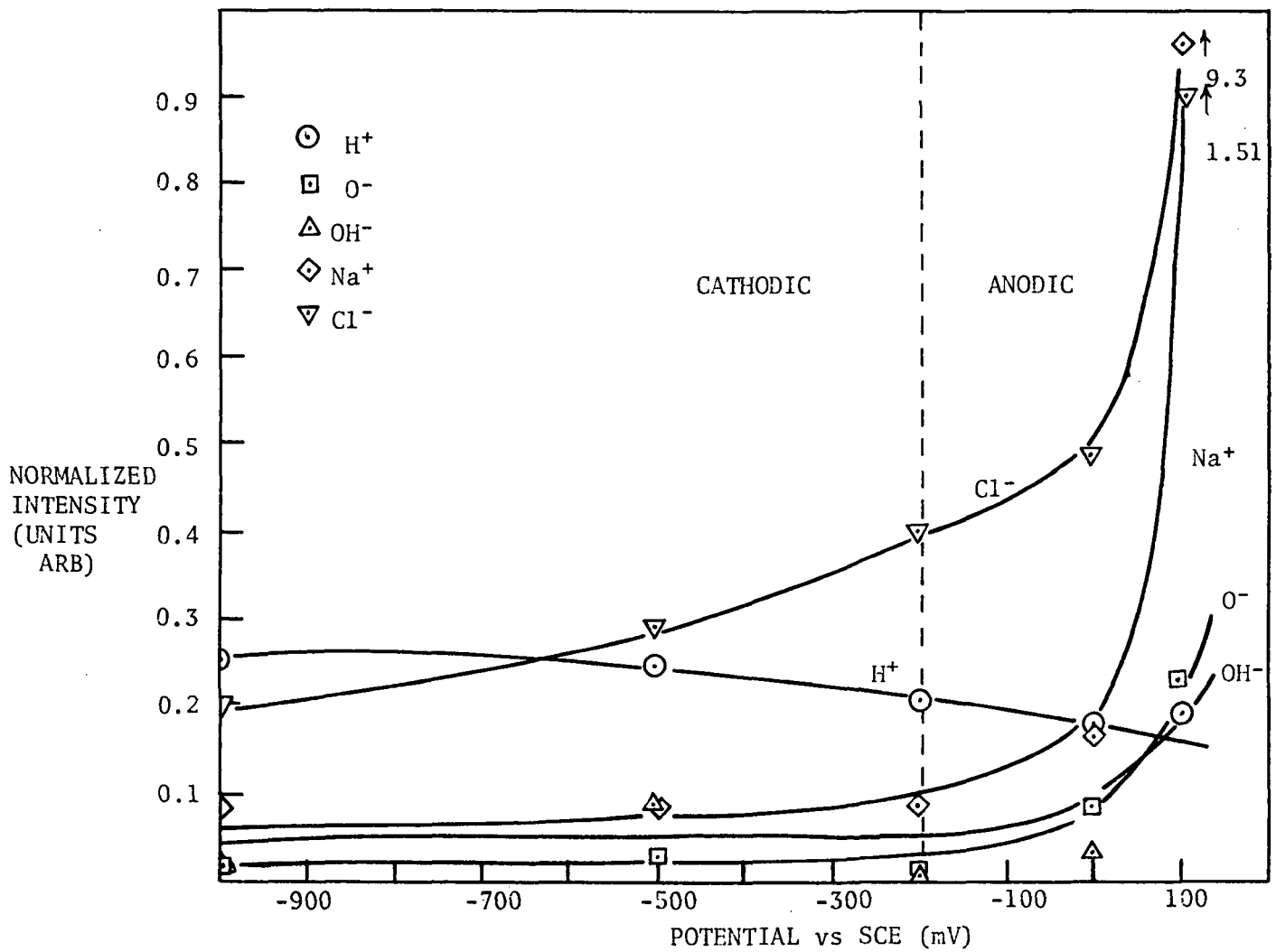

FIGURE 19: CONCENTRATION VS POTENTIAL FOR 310 STAINLESS STEEL IN 5M NaCl, AERATED AT 23°C.

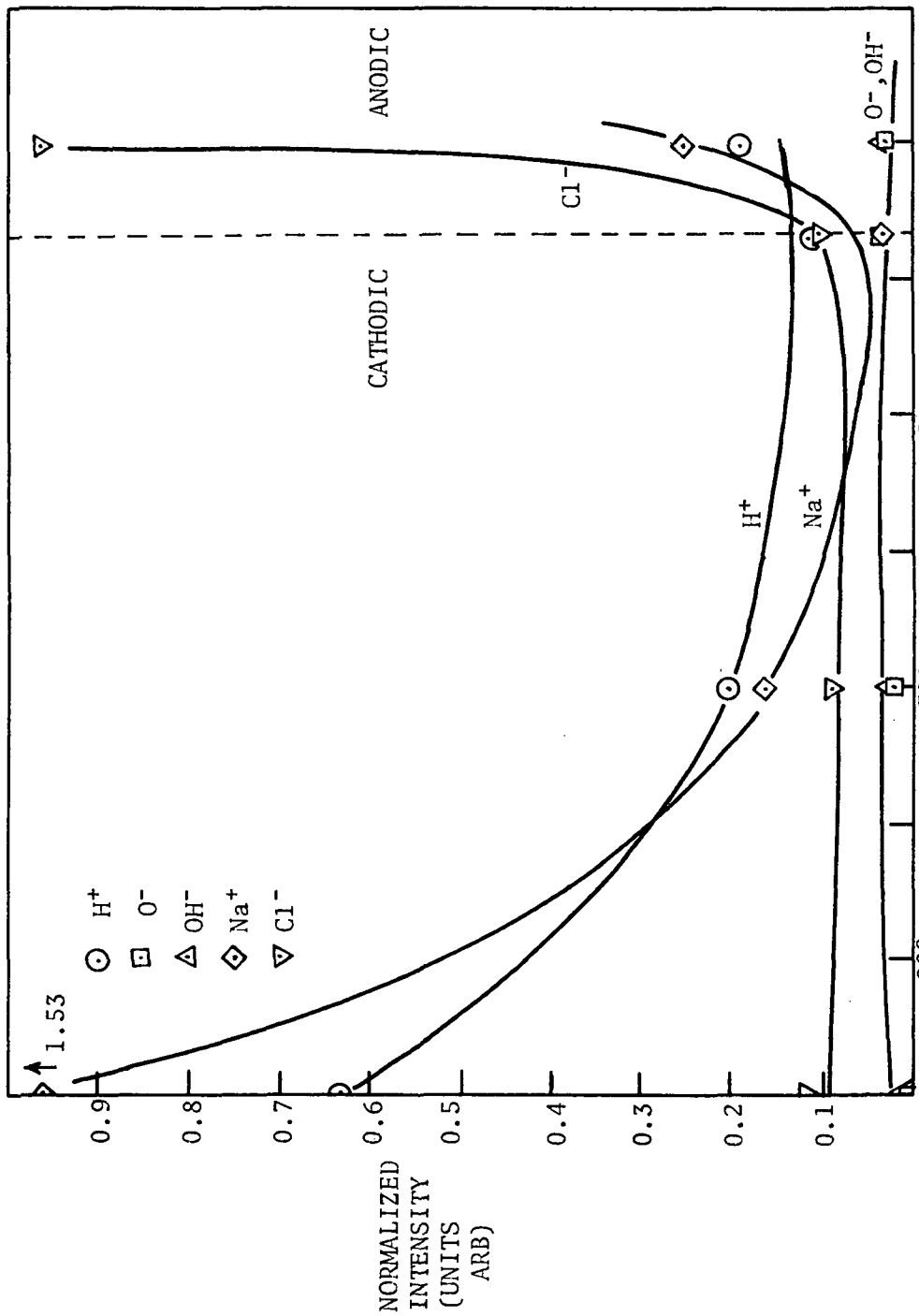

FIGURE 20a: CONCENTRATION VS POTENTIAL FOR 310 STAINLESS STEEL IN 5M NaCl AT 103°C.

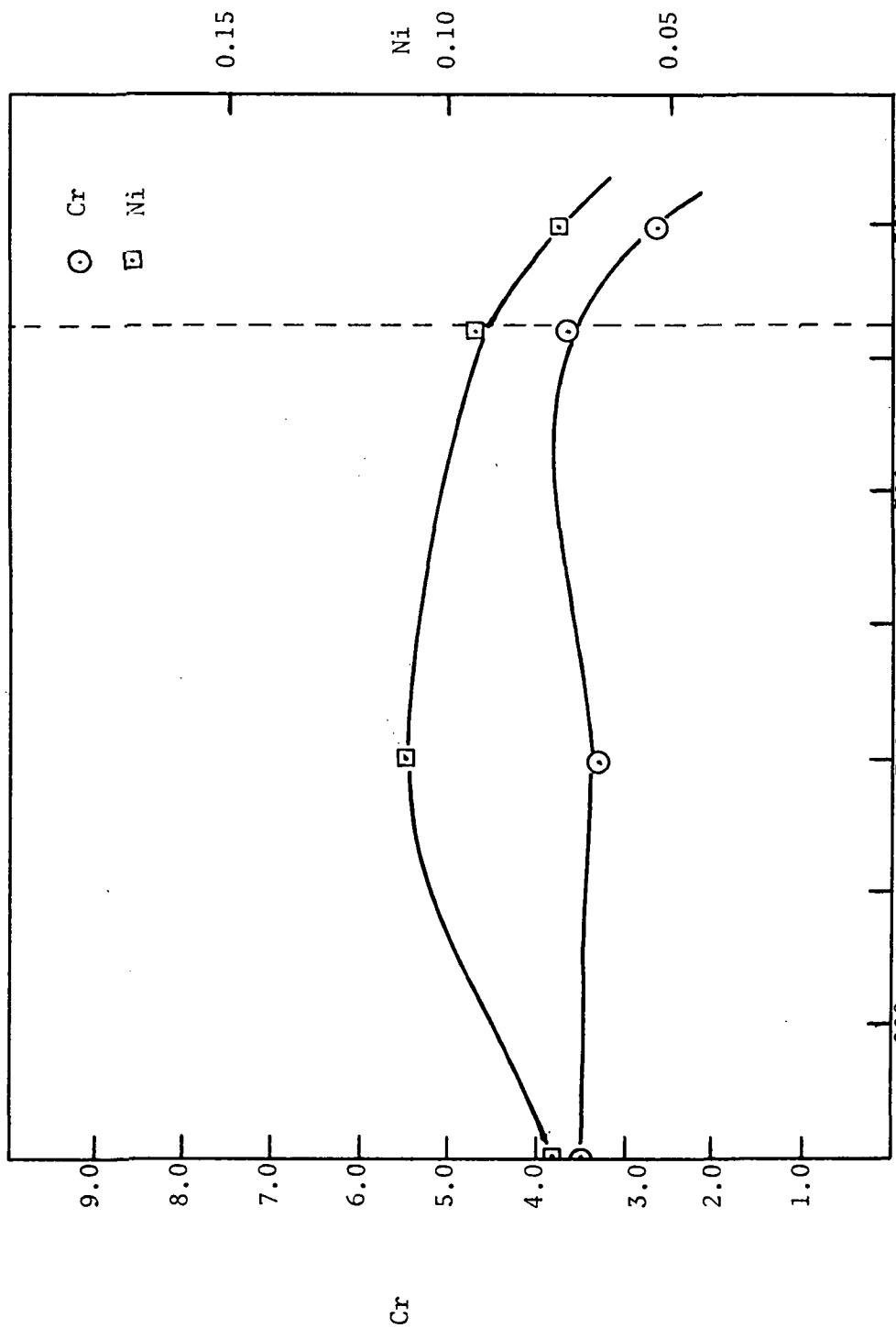

FIGURE 20b: CONCENTRATION VS POTENTIAL FOR 310 STAINLESS STEEL IN 5M NaCl AT 103°C.

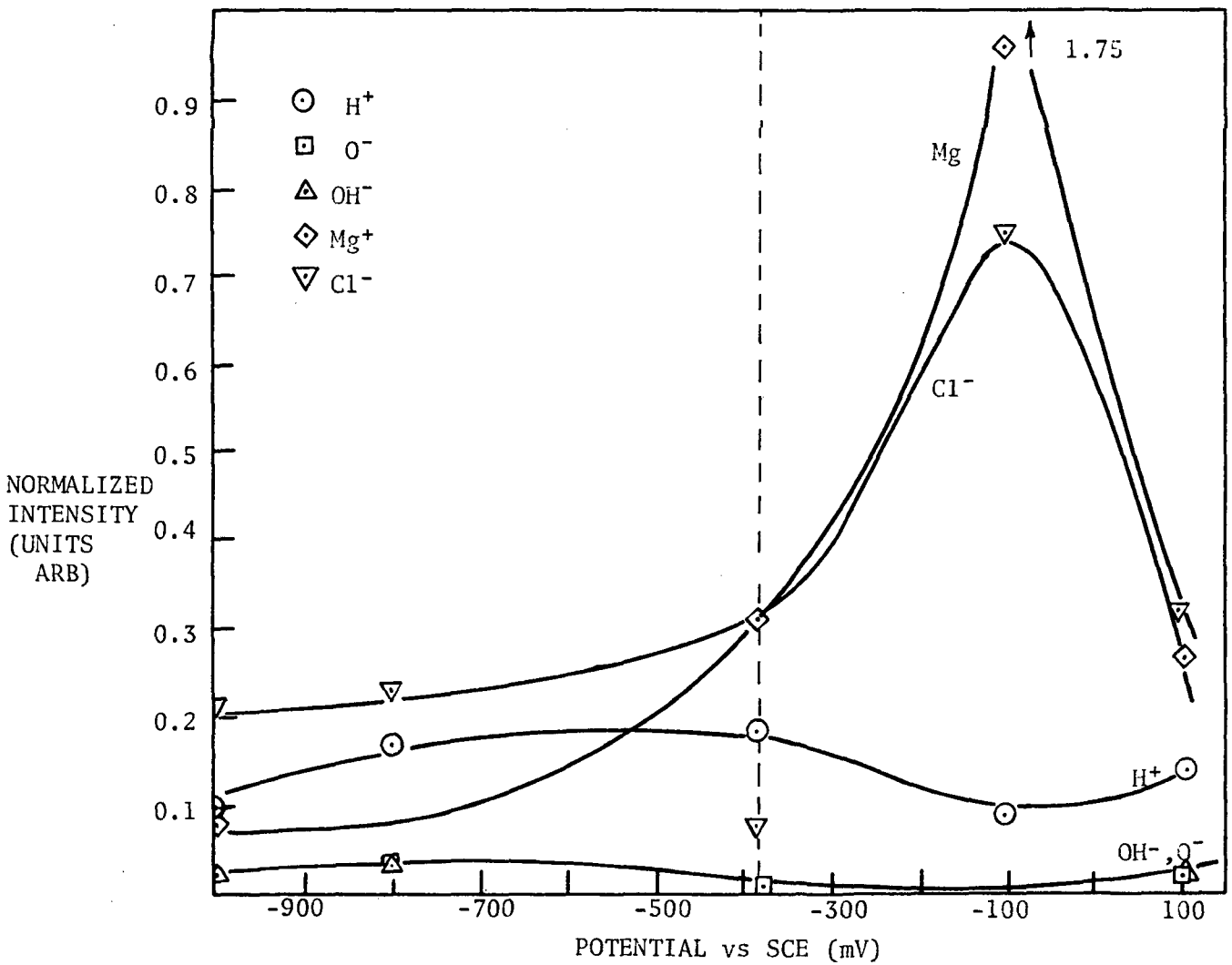

FIGURE 21a: CONCENTRATION VS POTENTIAL FOR 310 STAINLESS STEEL IN 2.5M $MgCl_2$, DEAERATED AT 23°C.

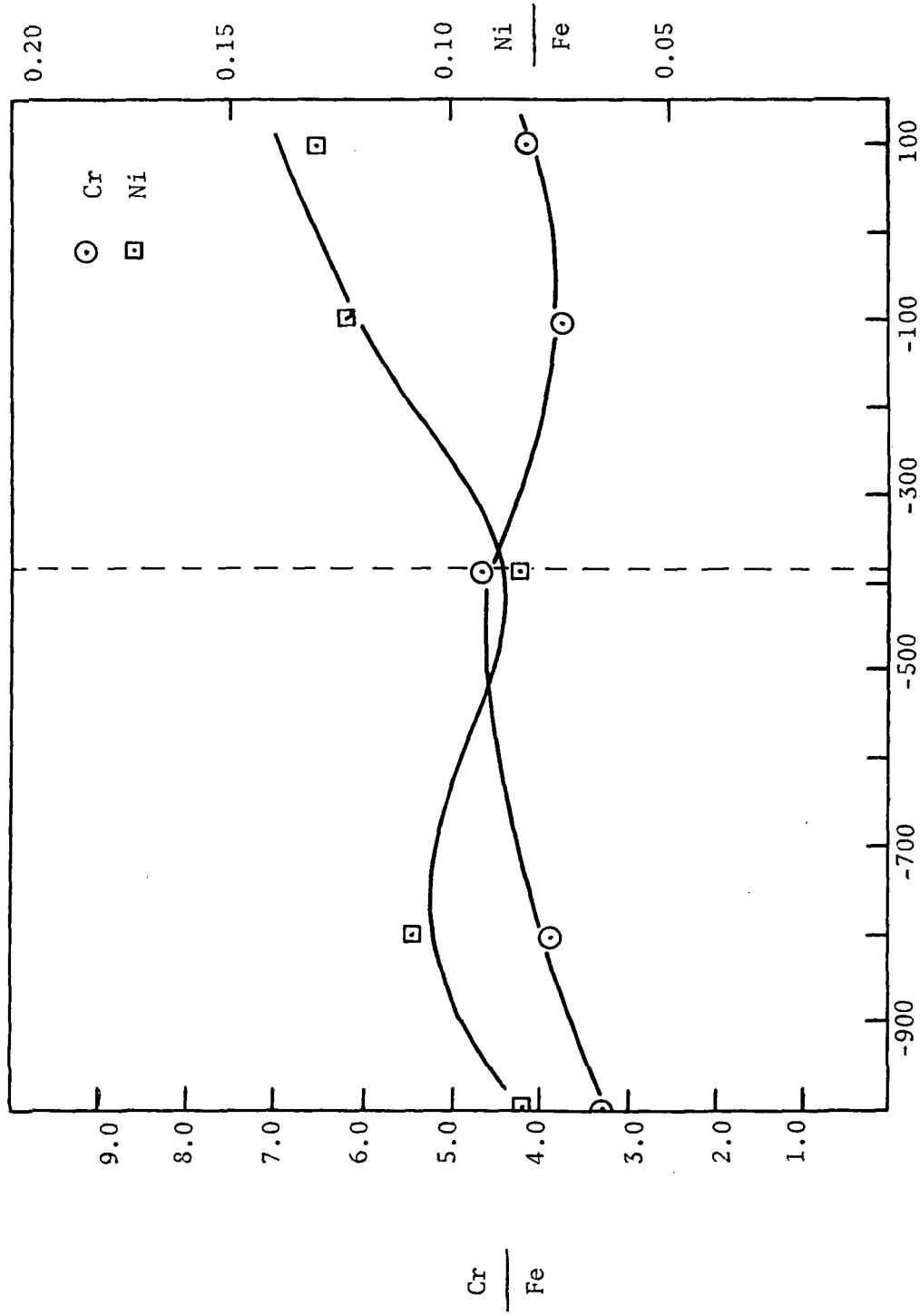

FIGURE 21b: CONCENTRATION VS POTENTIAL FOR 310 STAINLESS STEEL IN 2.5M MgCl2, DEAERATED AT 23°C.

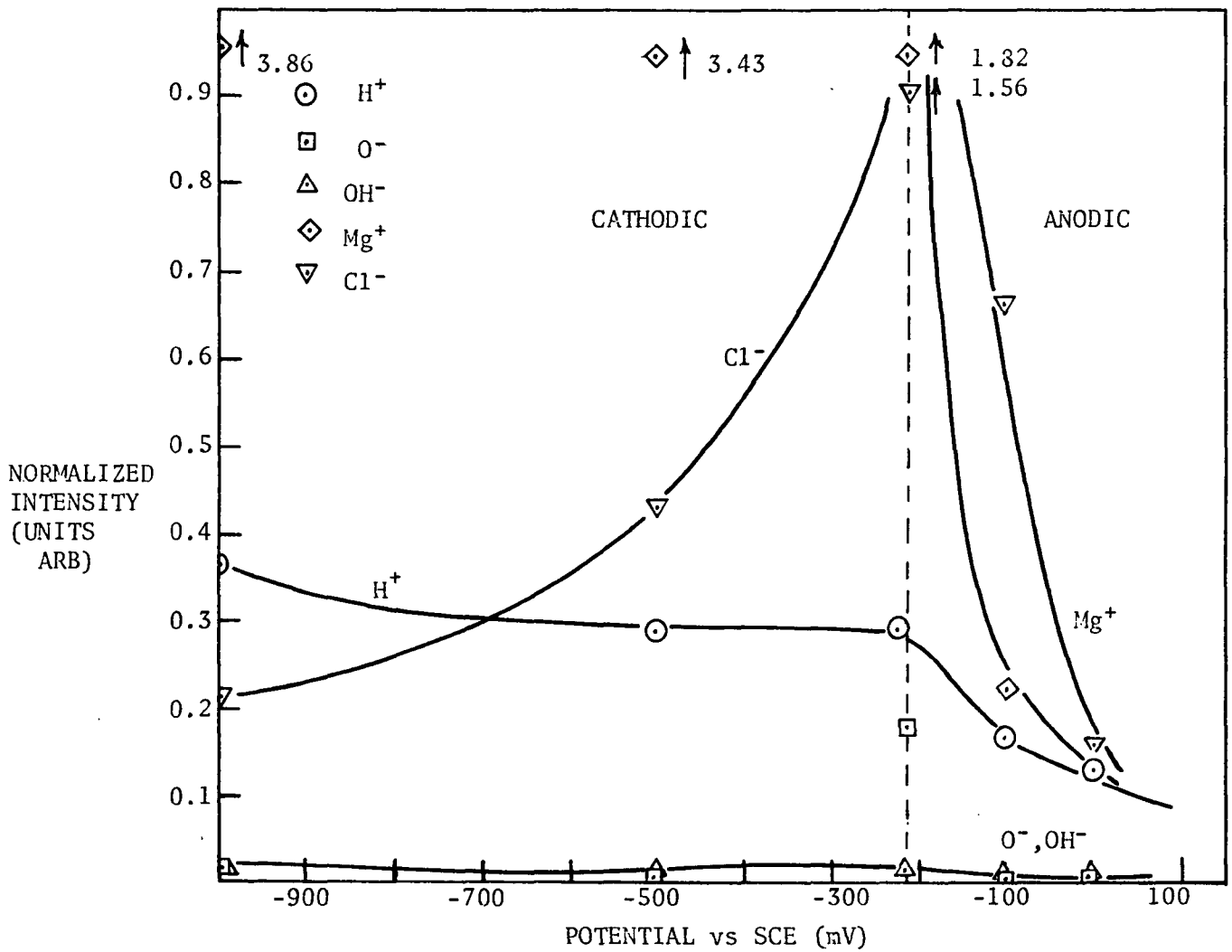

FIGURE 22: CONCENTRATION VS POTENTIAL FOR 310 STAINLESS STEEL IN 2.5M $MgCl_2$, AERATED AT 23°C.

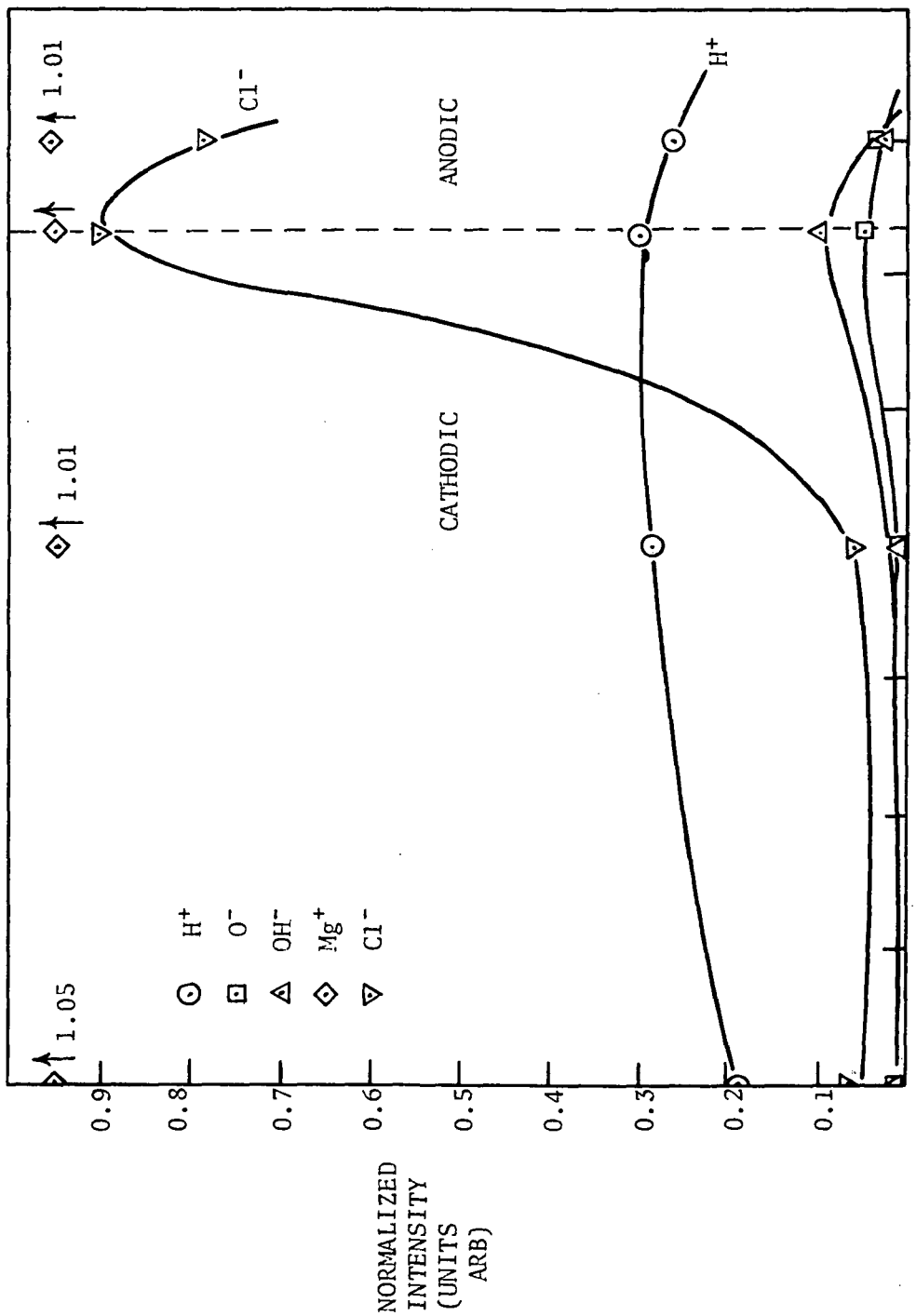

FIGURE 23a: CONCENTRATION VS POTENTIAL FOR 310 STAINLESS STEEL IN 2.5M MgCl2 AT 108°C.

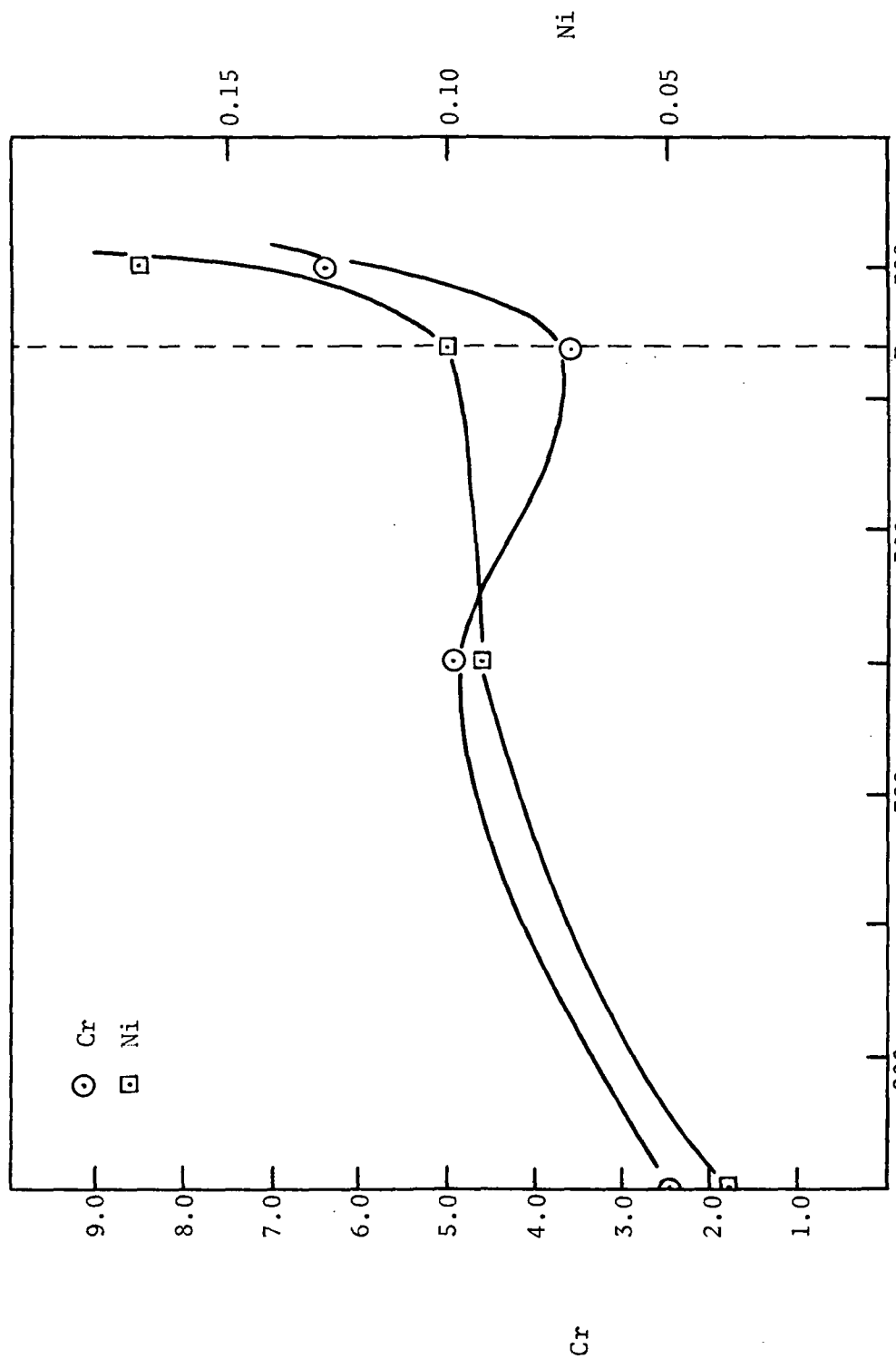

FIGURE 23b: CONCENTRATION VS POTENTIAL FOR 310 STAINLESS STEEL IN 2.5M $MgCl_2$ AT 108°C.

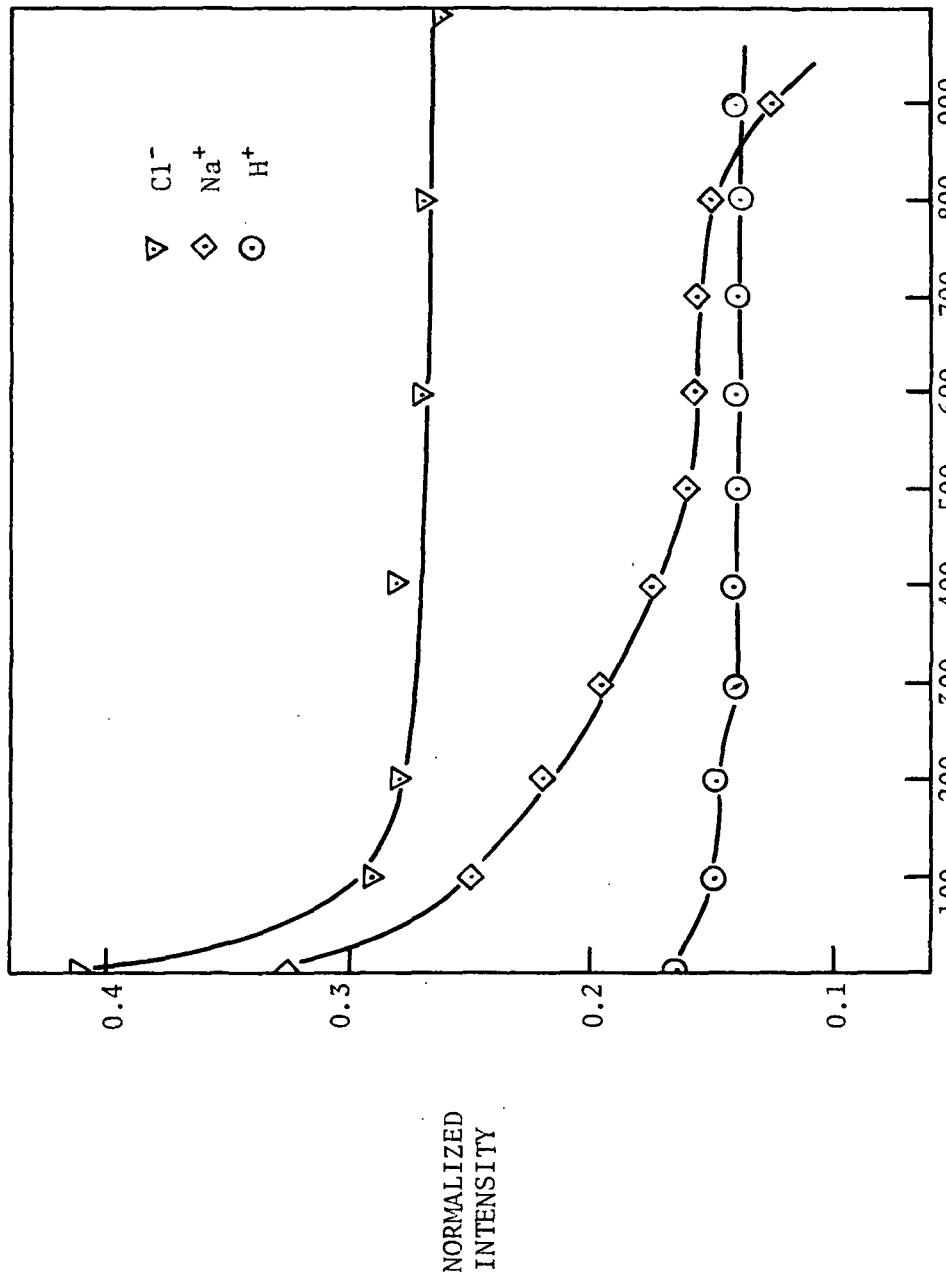

FIGURE 24: CONCENTRATION PROFILE OF ANODICALLY POLARIZED 310 STAINLESS STEEL IN 5M NaCl, DEAERATED AT 23°C AND UNSTRESSED.

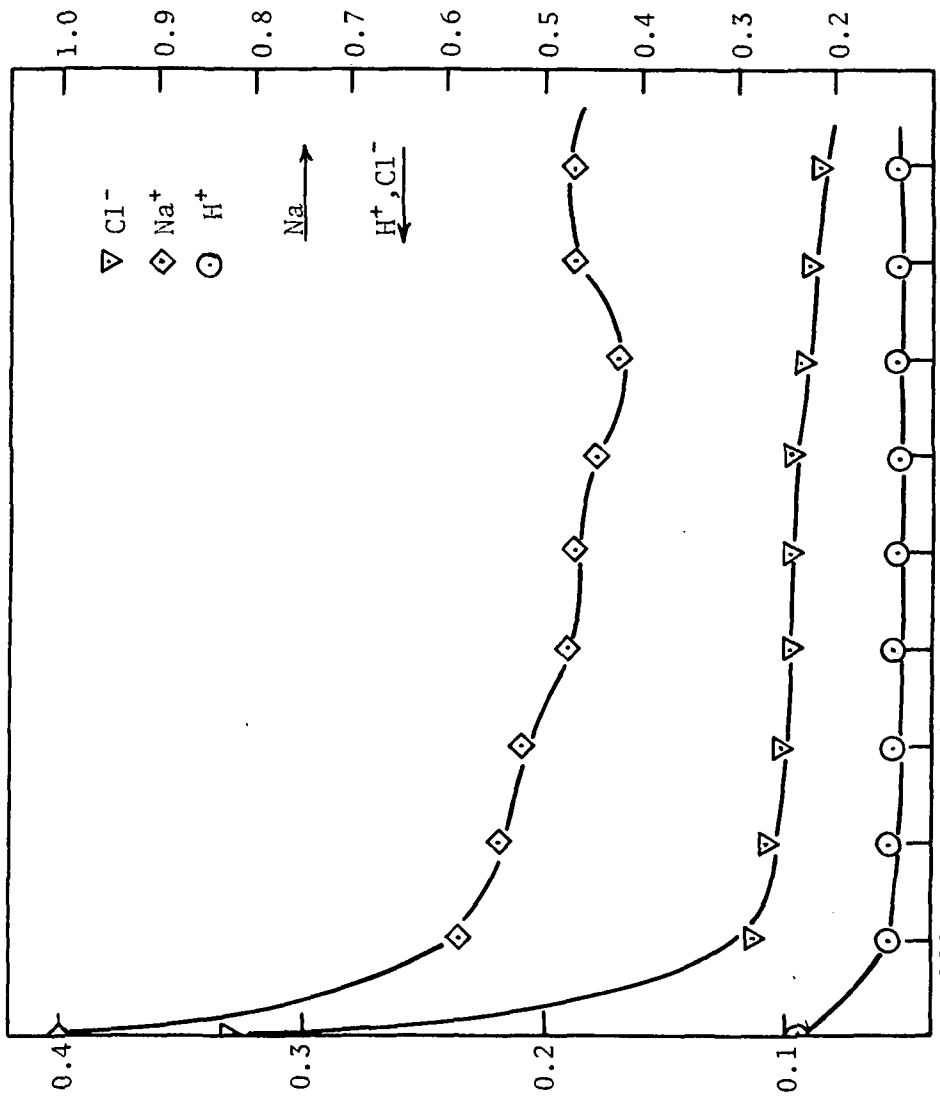

FIGURE 25: CONCENTRATION PROFILE OF ANODICALLY POLARIZED 310 STAINLESS STEEL IN 5M NaCl DEAERATED AT 23°C AND STRESSED AT THE YIELD POINT.

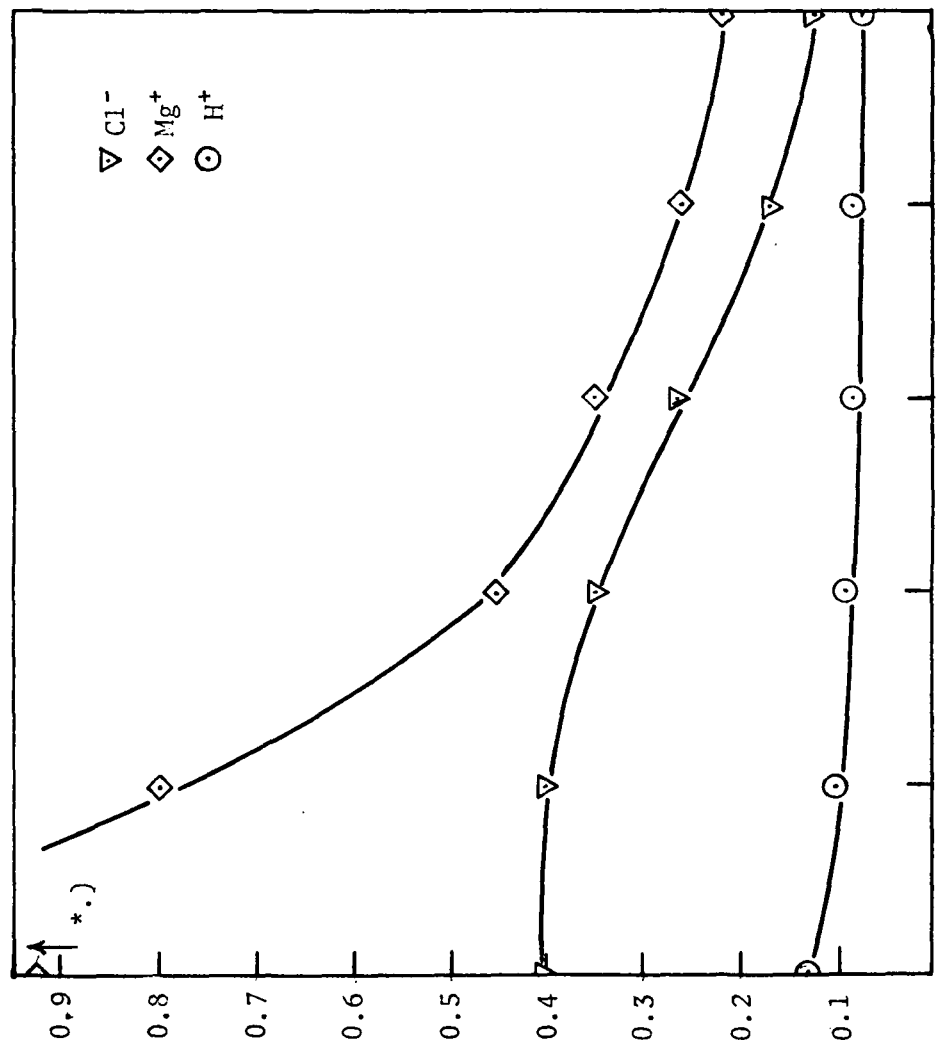

FIGURE 26: CONCENTRATION PROFILE FOR ANODICALLY POLARIZED 310 STAINLESS STEEL IN 2.5M $MgCl_2$ DEAERATED AT 23°C AND UNSTRESSED.

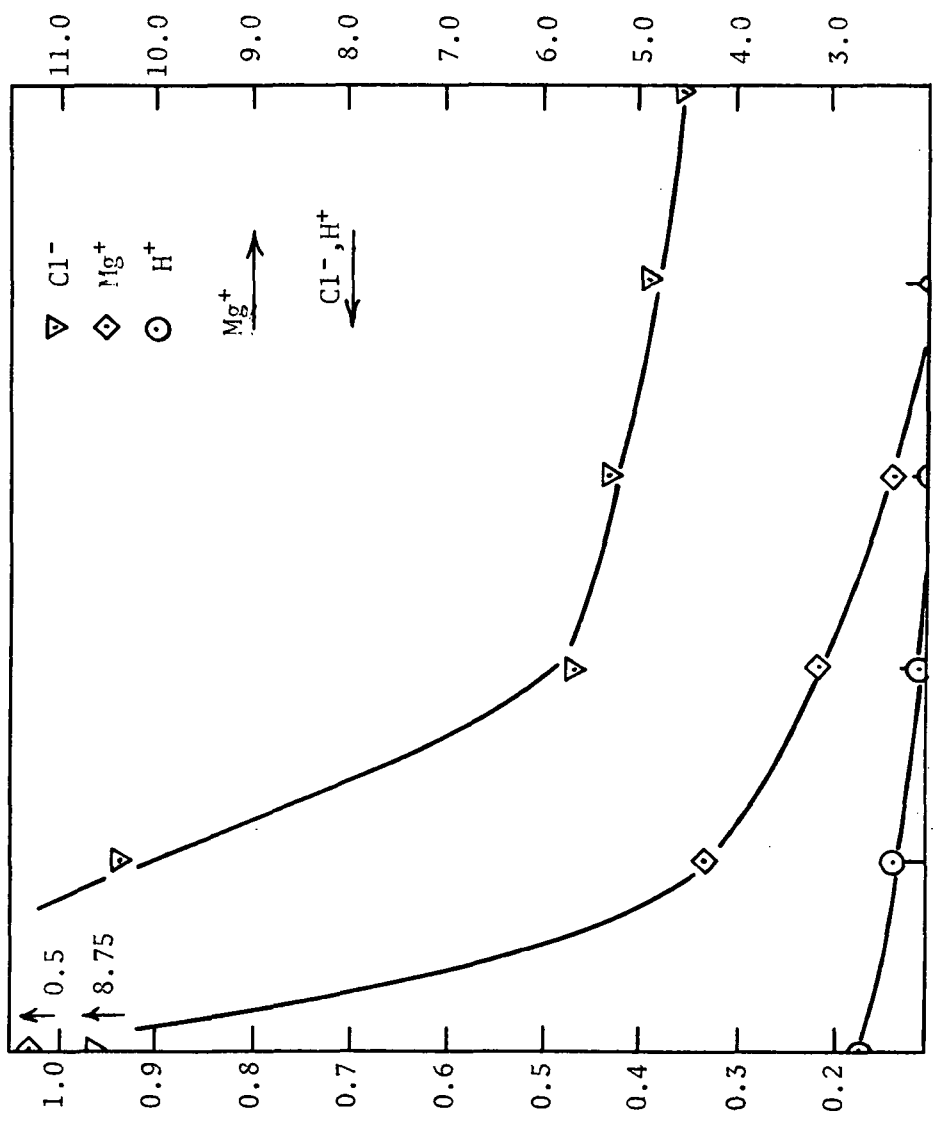

FIGURE 27: CONCENTRATION PROFILE FOR ANODICALLY POLARIZED 310 STAINLESS STEEL IN 2.5M $MgCl_2$ DEAERATED AT 23°C AND STRESSED AT THE YIELD POINT.

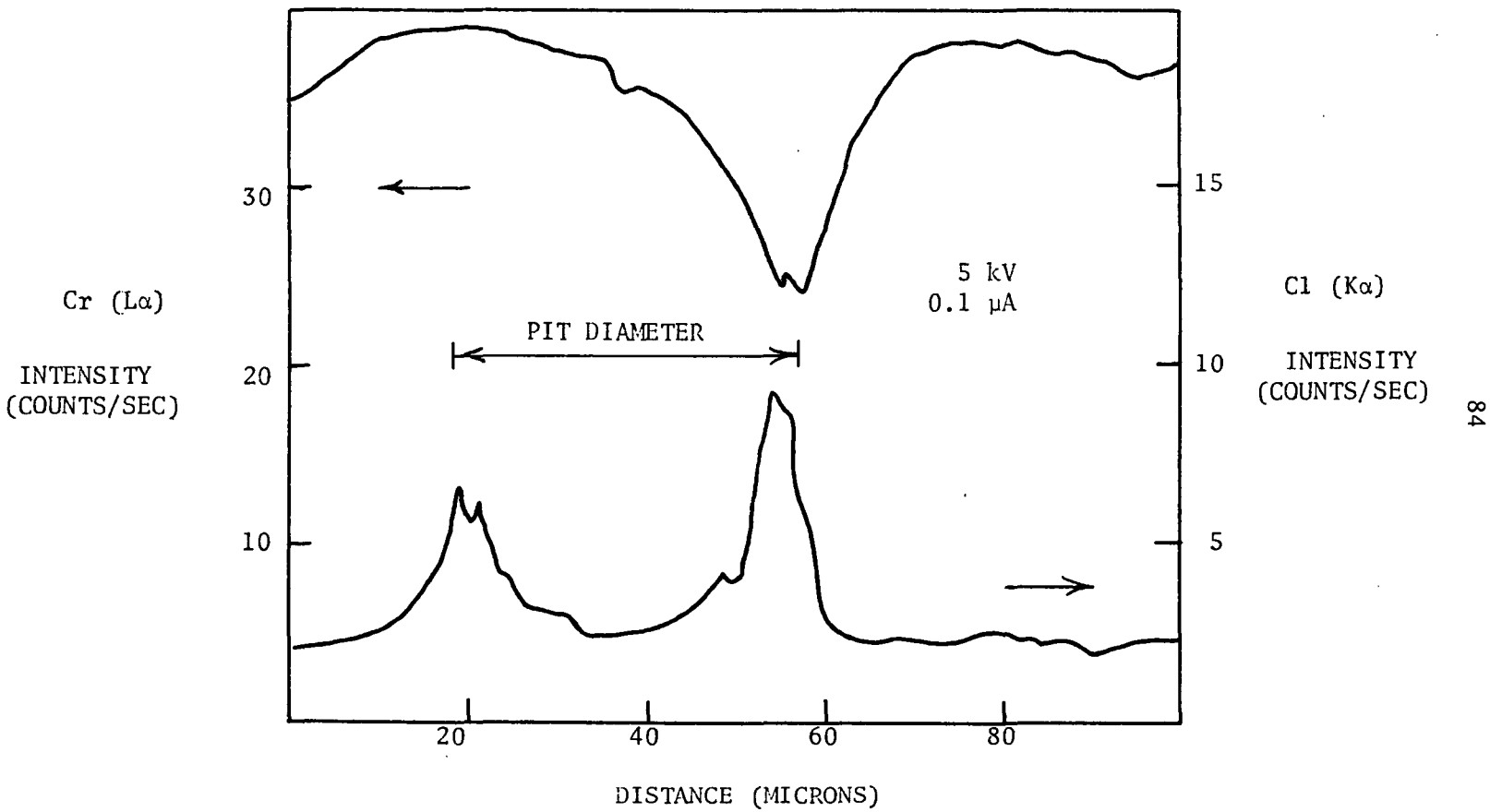

FIGURE 28: TYPICAL SPATIAL DISTRIBUTION OF Cr AND Cl AT A PIT.

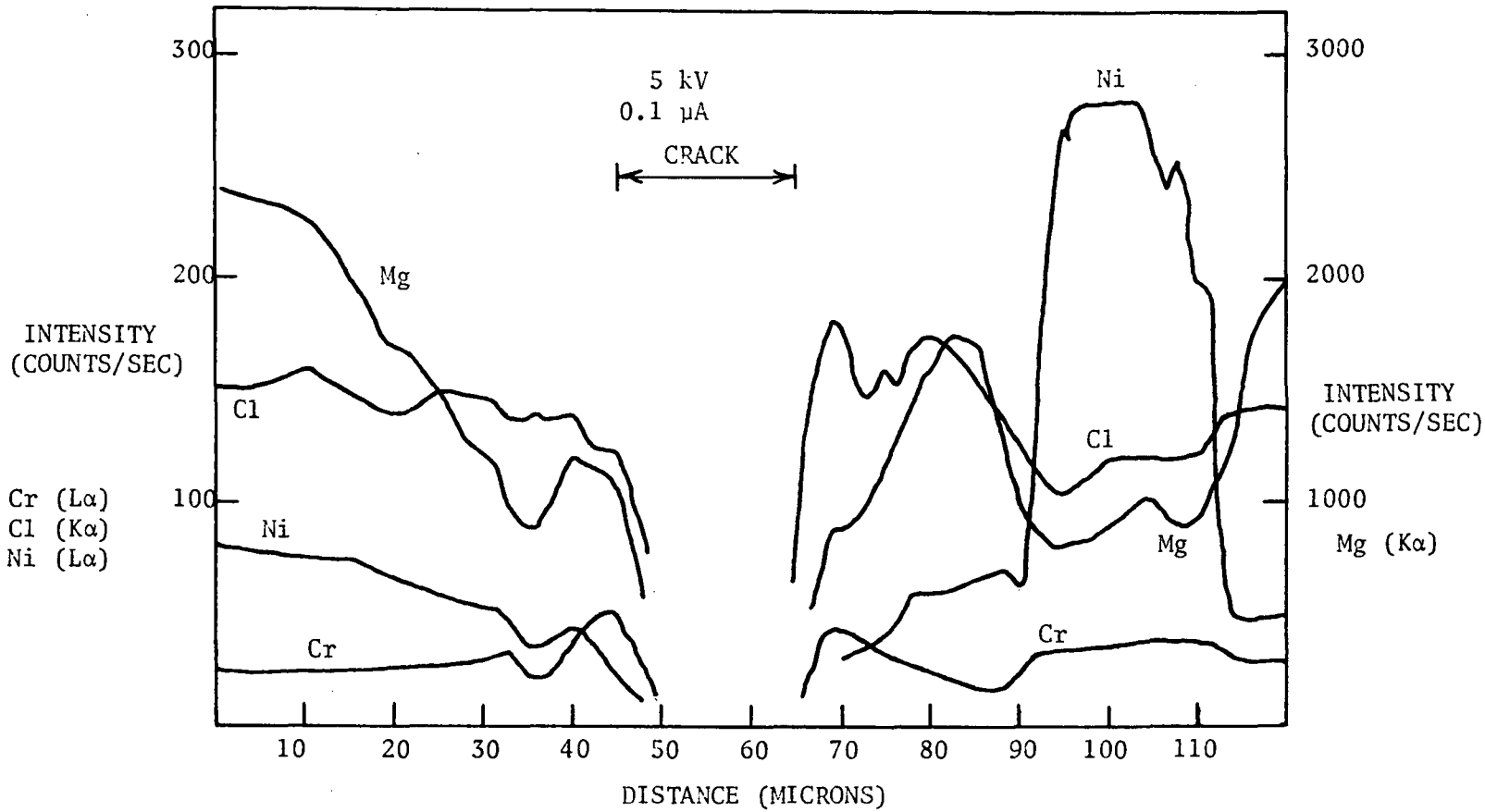

FIGURE 29: SPATIAL DISTRIBUTION OF Cl, Mg, Ni AND Cr AT A SECONDARY STRESS CORROSION CRACK.

FIGURE 30: SECONDARY CRACKS ON THE SURFACE OF 310 STAINLESS STEEL STRESS CORROSION CRACKED IN $MgCl_2$ AT 108°C, 1000X.

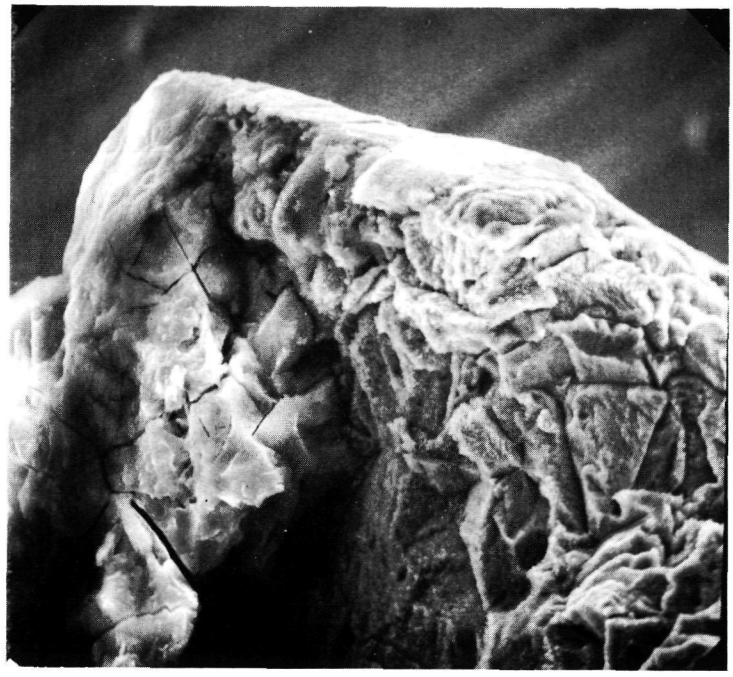

FIGURE 31: PRIMARY FRACTURE SURFACE OF THE STRESS CORROSION CRACKED 310 STAINLESS STEEL, 1000X.

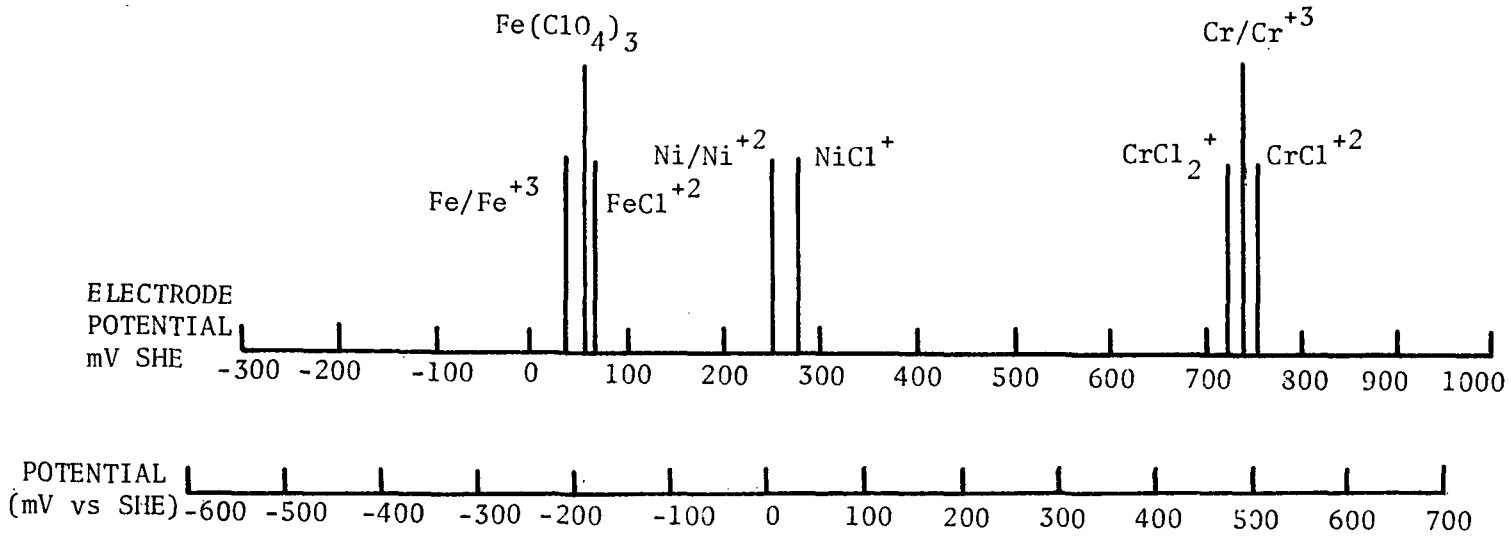

FIGURE 32: EQUILIBRIUM POTENTIALS FOR POSSIBLE SURFACE COMPLEXES FORMED DURING THE SCC OF AN AUSTENITIC STAINLESS STEEL IN AN AQUEOUS CHLORIDE ENVIRONMENT.

DR. JOHN TRUHAN (10)
DR. CHARLES W. ANDREWS (2)
DR. HUGH R. GRAY (1)
DR. RICHARD C ASHBROOK
DR. HUBERT B. PROBST
LIBRARY
REPORT CONTROL
NASA LEWIS RESEARCH
CENTER
21000 BROOKPARK ROAD
CLEVELAND, OHIO 44135

TECHNICAL LIBRARY
AFML/LAM
HEADQUARTERS
WRIGHT PATTERSON AFB
OHIO 45433

MR. J. MALTZ /RWM
MR. J. GANGLER /RWM
NASA HEADQUARTERS
WASHINGTON, D,C, 20546

DR. JOHN A. PETERSON
ARMCO STEEL CORPORATION
MIDDLETOWN, OHIO 45042

DR. HOWARD NELSON
DR. DELL WILLIAMS
NASA AMES RESEARCH
CENTER
MOFFETT FIELD, CAL. 94035

DR. JAMES DONOVAN
MR. M. R. LOUTHAN, JR.
E. I. duPONT deNEMOURS, INC.
SAVANNAH RIVER LABORATORY
AIKEN, SOUTH CAROLINA 29801

MR. C. E. CATALDO
MR. W. B. McPHERSON
NASA MARSHALL SPACECRAFT
CENTER
HUNTSVILLE, ALABAMA 35812

DR. W. T. CHANDLER
MR. R. J. WALTER
NORTH AMERICAN ROCKWELL
ROCKETDYNE DIVISION
6633 CANOGA AVENUE
CANOGA PARK, CAL. 91304

MR. R. E. JOHNSON
MR. ROYCE FORMAN
NASA JOHNSTON SPACE CENTER
HOUSTON, TEXAS 77058

DEFENSE DOCUMENTATION CENTER
CAMERON STATION
5010 DUKE STREET
ALEXANDRIA, VIRGINIA 22314

DR. RAY B. BENSON
DEPARTMENT OF METALLURGY
NORTH CAROLINA STATE
UNIVERSITY
RALEIGH, NORTH CAROLINA
27601

PROFESSOR R. P. WEI
DEPT. OF MECHANICAL
ENGINEERING & MECHANICS
LEHIGH UNIVERSITY
BETHLEHEM, PA. 18015

MR. J. A. ALEXANDER
MATERIALS TECHNOLOGY
TRW - EQUIPMENT GROUP
23555 EUCLID AVENUE
CLEVELAND, OHIO 44117

DR. LOUIS RAYMOND
AEROSPACE CORPORATION
BLDG. 130, ROOM 2281
P.O. BOX 95085
LOS ANGELES, CAL. 90045

MR. C. D. BEACHEM
NAVAL RESEARCH LABORATORY
WASHINGTON, D.C. 20390

MR. T. P. GROENEVELD
BATTELLE MEMORIAL INST.
505 KING AVENUE
COLUMBUS, OHIO 43201

DR. ANTHONY THOMPSON
DR. NEIL PATON
ROCKWELL SCIENCE CENTER
THOUSAND OAKS, CAL. 91360

MR. E. JANKOWSKY
Ms. SARAH KETCHAN
NAVAL AIR DEVELOPMENT
CENTER
WARMINSTER, PA. 18974

DR. E. A. STEIGERWALD
TRW - METALS DIVISION
MINERVA, OHIO 44657

DR. JOHN A. HARRIS, JR.
PRATT & WHITNEY RESEARCH
CENTER
WEST PALM BEACH, FLA. 33402

DR. E. N. MARSH
VICE PRESIDENT
RESEARCH & ENGINEERING
STANDARD OIL CO. OF OHIO
MIDLAND BUILDING
CLEVELAND, OHIO 44115

DR. FRED RADD
CONTINENTAL OIL CO.
PONCA CITY, OKLAHOMA 74601

DR. H. H. JOHNSON
CORNELL UNIVERSITY
DEPARTMENT OF METALLURGY
ITHACA, NEW YORK 14850

DR. I. M. BERNSTEIN
CARNEGIE MELLON UNIVERSITY
PITTSBURGH, PA. 15213

MR. J. P. FIDELLE
FRENCH ATOMIC ENERGY
COMMISSION
BRUYERES - 1e - CHATEL
91680, FRANCE

DR. G. C. SMITH
UNIVERSITY OF CAMBRIDGE
PEMBROKE STREET
CAMBRIDGE, UK CB 2 3QZ
ENGLAND

DR. R. A. ORIANI
U. S. STEEL RESEARCH LABS.
MONROEVILLE, PA. 15146

DR. JOHN KOCHERA
SHELL DEVELOPMENT CO.
P. O. BOX 481
HOUSTON, TEXAS 77001

DR. DAVID ELMER
STANDARD OIL OF CALIF.
P. O. BOX 1272
RICHMOND, CAL. 94802

DR. TOM SCOTT
METALS DEVELOPMENT BLDG.
IOWA STATE UNIVERSITY
AMES, IOWA 50011

DR. ALAN S. TETELMAN
UCLA-DEPT. OF METALLURGY
LOS ANGELES, CAL. 90024

DR. DONALD STEVENS
ASSISTANT DIRECTOR
PHYSICAL RESEARCH
THE ATOMIC ENERGY COMMISSION
GERMANTOWN, MARYLAND

DR. A. O. SCHAEFER, DIRECTOR
METALS PROPERTY COUNCIL
UNITED ENGINEERING CENTER
345 EAST 47TH STREET
NEW YORK, NEW YORK 10017

DR. RAY DECKER, DIRECTOR
RESEARCH & DEVELOPMENT
THE INTERNATIONAL NICKEL
COMPANY
ONE NEW YORK PLAZA
NEW YORK, NEW YORK 10004

DR. EDWARD WRIGHT, CHIEF
MATERIALS ENGINEERING
ARMY MATERIALS RESEARCH
CENTER
WATERTOWN, MASSACHUSETTS
02172

DR. W. J. McGUIRE
GULF RESEARCH AND
DEVELOPMENT
P. O. BOX 2038
PITTSBURGH, PA. 15230

DR. H. E. JOHNSON
EXXON PRODUCTION RESEARCH
COMPANY
P. O. BOX 2189
HOUSTON, TEXAS 77001

NASA (10)
SECURITY AND TECHNICAL
INFORMATION FACILITY
ACQUISITIONS BRANCH
P. O. BOX 33, COLLEGE PARK
MARYLAND 20740

K. B. DAS
THE BOEING COMPANY
P. O. BOX 3999
SEATTLE, WASHINGTON 98124

P. N. ADLER
RESEARCH DEPARTMENT
GRUMMAN AEROSPACE CORPORATION
BETHPAGE, NEW YORK 11714

A. H. MILLER
DeLAVAL TURBINE, INC.
853 NOTTINGHAM WAY
TRENTON, NEW JERSEY 08602

R. F. HERZOG
DEPARTMENT OF PHYSICS
UNIVERSITY OF SOUTHERN
MISSISSIPPI
HATTIESBURG, MISSISSIPPI
39401

C. A. ANDERSON
HASLER RESEARCH CENTER
APPLIED RESEARCH LABORATORIES
COLETA, CAL.